Effect of the location pattern of rural residential buildings on natural ventilation in mountainous terrain of central China

Xie, Mingjing; Wang, Yuran; Liu, Zhengxuan; Zhang, Guoqiang

DOI
10.1016/j.jclepro.2022.130837

Publication date
2022

Document Version
Final published version

Published in
Journal of Cleaner Production

Journal of Cleaner Production 340 (2022) 130837

Contents lists available at ScienceDirect

Journal of Cleaner Production

journal homepage: www.elsevier.com/locate/jclepro

Effect of the location pattern of rural residential buildings on natural ventilation in mountainous terrain of central China

Mingjing Xie [a], Yuran Wang [a], Zhengxuan Liu [a,b,c,*], Guoqiang Zhang [b]

[a] School of Architecture and Art, Central South University, Changsha, 410012, China
[b] National Center for International Research Collaboration in Building Safety and Environment, Hunan University, Changsha, 410082, China
[c] Faculty of Architecture and the Built Environment, Delft University of Technology, Julianalaan 134, 2628 BL, Delft, the Netherlands

ARTICLE INFO

Handling Editor: M.T. Moreira

Keywords:
Hilly terrains
Rural residential buildings
Location pattern
Natural ventilation
Wind tunnel experiment
CFD simulation

ABSTRACT

The use of natural ventilation in buildings to reduce the energy consumption and CO_2 emission has been widely investigated and practiced, but few existing studies have considered the exploration and assessment of natural ventilation in different location patterns of rural residential buildings in the mountainous terrain of China. In this paper, the representative rural residential buildings are firstly selected in Huarong, Pingjiang and Liuyang regions of northern Hunan Province to carry out on-site survey works to determine building types, physical parameters and layout forms. Then, the wind tunnel experiments are carried out to investigate the effectiveness of natural ventilation under different location patterns, and the monitored results are compared with simulated data. The results show that the experiments and simulations are in satisfactory agreement. The experimental data also indicate that when the modelled distance of 120 mm (i.e. 12 m between the building and hilly terrain in practical application) is the best option for building natural ventilation. Based on the investigation and statistical data, the natural ventilation effectiveness under different location patterns and operational conditions is simulated using CFD methods, and it is obtained the most favourable location pattern for natural ventilation. The results show that the winter ventilation of buildings in the existing location pattern is significantly obstructed in the hilly terrain, which is favourable to the indoor thermal environment, however, the natural ventilation is compromised to a certain extent in summer. Furthermore, the findings also show that, regardless of the hilly terrain's height at 50 m or 150 m, the buildings are able to avoid natural ventilation in winter to the maximum extent when the distance between the buildings and the frontier of the hilly terrain is double that of the building height (i.e. 12 m). This study could contribute to theoretical instructions for optimum design of natural ventilation of rural residential buildings in the mountainous terrain of central China.

1. Introduction

Energy consumption in buildings accounts for a large proportion of the total energy consumption in all countries, with the proportion being at over 30% (Huo et al., 2018). In particular, this proportion has reached 40% in developed countries like the EU and USA (Liu et al., 2018). In China, rural residential buildings account for a large proportion of the total buildings, and thus the energy consumption of rural residential buildings is an issue that requires significant attention (Ma et al., 2020). Due to the economic constraints, the emphasis of energy conservation of rural buildings lies in more appropriate utilization of low-cost passive technologies that can effectively improve indoor thermal environment. In order to create an indoor thermal environment that is harmonious for human habitation without increasing energy consumption (Li et al., 2020; Zhang et al., 2020). The utilization of passive technologies can minimize or eliminate the use of refrigeration and heating equipment, as well as creating a comparatively high-quality indoor and outdoor environment. As a representative of hot summer and cold winter regions in China, the critical aspect of building conservation in Hunan Province is to lower the energy consumption caused by improving indoor thermal environment in summer and winter. Natural ventilation, as the most common passive energy-saving technology, has been widely used and promoted in practical engineering due to its advantages of low-energy consumption, low-cost, low-maintenance and high air quality (Chen et al., 2020; Miri and Babakhani, 2021).

The rationalization of natural ventilation in different regions and building types has been one of passionate research topics in the field of

* Corresponding author. Faculty of Architecture and the Built Environment, Delft University of Technology, Julianalaan 134, 2628 BL, Delft, the Netherlands.
E-mail addresses: Z.liu-12@tudelft.nl, zhengxuanliu@hnu.edu.cn (Z. Liu).

https://doi.org/10.1016/j.jclepro.2022.130837
Received 11 November 2021; Received in revised form 18 January 2022; Accepted 2 February 2022
Available online 4 February 2022

Abbreviations

C_μ	Coefficients in approximated turbulent transport equations
L_O	Qualitative length
K	Turbulent kinetic energy after dimensionless
R_e	Reynolds number
U_0	Average wind speed in a horizontal direction at any height
U_i	Dimensionless velocity component in the i direction
U_Z	Average wind speed in horizontal direction under standard reference height
$\overline{u_j}$	Velocity component in j direction
ν_t	Turbulent kinetic energy viscosity coefficient
x_j	Cartesian co-ordinates in j direction
Z_0	Any height
ρ	Air density
CFD	Computational fluid dynamics
E	Turbulent energy viscous dissipation rate after dimensionless
k	Turbulent kinetic energy
P	Average shear stress after dimensionless
t	Flow time
ε	Turbulent energy viscous dissipation rate
U_j	Dimensionless velocity component in the j direction
$\overline{u_i}$	Velocity component in i direction
ν	Kinetic energy viscosity
x_i	Cartesian co-ordinates in i direction
Z	Standard reference height
α	Ground roughness index
Γ_{seff}	Effective diffusion coefficient for turbulent energy dissipation rate
TFI	Turbulent flow instrumentation

building energy efficiency and indoor thermal environment improvement (Lyu et al., 2021; Meng et al., 2020; Wu et al., 2021). The fundamental driving forces of natural ventilation include wind pressure and thermal pressure driving. Wind pressure refers to the pressure difference between the windward and leeward sides when the outdoor atmospheric movement impinges on the buildings, thereby generating the power to drive indoor airstream movement. Thermal pressure is the force that drives airflow movement due to the gravitational difference generated by the temperature difference between the internal and external atmosphere. In buildings, wind pressure driving forces generally form natural ventilation in the horizontal direction, while thermal pressure forms natural ventilation in the vertical direction (Sakiyama et al., 2021; Zhang et al., 2021). Many academics have conducted numerous studies on natural ventilation by thermal pressure in different types of buildings and natural ventilation by the combined effect of thermal pressure and wind pressure. Their specific research areas mainly involve the following respects: i) design and optimization of natural ventilation in office buildings (Nomura and Hiyama, 2017); ii) performance evaluation of natural ventilation design integrated into the entire design process of multi-story buildings (Omrani et al., 2017); iii) effects of balcony geometry on natural ventilation performance and occupant perception in mid-and high-rise residential buildings (Izadyar et al., 2020); iv) factors influencing natural ventilation performance of building wind catchers (including internal geometry, external architectural characteristics, and surrounding environment) (Jomehzadeh et al., 2020); v) assessment of indoor air quality and thermal comfort by passive cooling of building natural ventilation wind catchers (Jomehzadeh et al., 2017).

The research methods for natural ventilation of buildings are mainly divided into two categories: computational methods and wind tunnel experimental methods. The computational method has become the mainstream analytical evaluation method, because it is more straightforward than the wind tunnel experiment. And the design solution can be optimized more easily, as well as being more economical. Computational methods for natural ventilation mainly include analytical solution models, empirical models, multi-zone models, regional models, and CFD models (Larsen et al., 2018; Ledo Gomis et al., 2021). With the international energy organization's project Annex 35, computational methods are increasingly being applied to natural ventilation design (Heiselberg, 2002). Among them, CFD numerical simulation and multi-area network models are the most widely used, and many studies have also verified the accuracy and effectiveness of this method (Shafiei Fini and Moosavi, 2016).

In terms of natural ventilation evaluation, researchers generally start from the actual ventilation effect of buildings, based on the following two aspects: air quality and thermal comfort. Air quality is mainly related to the indoor air exchange rate, while thermal comfort has a broader range of influencing factors. Regarding indoor air quality under natural ventilation conditions, Vassella et al. (2021) and Schulze et al. (2018) respectively studied the influence of natural ventilation in school buildings and office buildings. They proposed control strategies and application measures to improve indoor air quality. Regarding indoor thermal comfort under natural ventilation conditions, Han et al. (2009) investigated and analyzed the thermal environment of naturally ventilated houses and thermal comfort states of residents in China's hot summer and cold winter regions. They established a quantitative thermal comfort model and comfort zone for naturally ventilated environments using statistical and artificial neural network methods, and proposed a thermal comfort equation under natural ventilation conditions in hot summer and cold winter regions of China. In addition, the researchers also carried out the investigations on natural ventilation airflow testing methods and conducted in-depth analyses on the applicability and reliability of different tracer gas methods (Remion et al., 2019).

At a more macro perspective, some researchers have also considered climatic regions as an access point to study natural ventilation. They primarily investigate the effectiveness of natural ventilation and ventilation design strategies under different urban planning and building layout scenarios. For example, Yang et al. (2021) investigated the contribution of natural ventilation to the urban thermal environment and energy demand under different climatic circumstances. Results showed that the improved ventilation could contribute directly or indirectly to reducing urban energy consumption, with up to a 6.704% reduction of energy demand in well-ventilated areas. He et al. (2015) studied the influences of urban planning and urban construction on natural ventilation, and evaluated the comprehensive influence of natural environment and typical urban morphological characteristics on urban heat load and ventilation potential. Based on the research results, the useable urban heat island mitigation measures and climate space planning guidelines were proposed to improve urban climate conditions.

As can be seen from the above studies, natural ventilation has been extensively investigated as one of the most promising passive technologies for energy saving applications in buildings (Aflaki et al., 2015; Calama-González et al., 2022). However, existing studies have mainly focused on the application of natural ventilation in urban buildings and urban planning, especially for medium and high-rise residential buildings in cities and wind environments within residential communities in different localities. In recent years, although some researchers have carried out studies on the potential of natural ventilation and design strategies for buildings in rural regions (Stavrakakis et al., 2010). However, few researchers have carried out in-depth investigations related to natural ventilation in rural residential buildings of hilly terrains. It is important to note that rural residential buildings in hilly

terrains are different from urban buildings and rural buildings in the plains for building surroundings, building layout, and wind environment formation mechanisms. However, literatures show that the ineffectiveness of natural ventilation causes health hazards in rural residential buildings of hilly terrains that should not be ignored. For example, rural energy facilities and utilization methods in Hunan Province, China are generally backward. The conventional biomass energy is not used efficiently, and the emission of large amounts of soot and ash is deteriorating the indoor air environment (Shan et al., 2015). Based on this, this paper carries out a measurement and simulation study of the natural ventilation performance of rural residential buildings in hilly terrains of China under different location patterns, with the improvement of natural ventilation performance as the overarching objective.

The innovation and contribution of this paper mainly include: 1) The research content of this study, as a new exploration theme, focuses on the natural ventilation investigation and analysis of rural residential buildings under different locations in the hilly terrains of Hunan Province. And the rationalization and improvement suggestions for the location selection of rural residential buildings are proposed based on the investigative results. 2) Based on the field investigation work, the design characteristics and location forms of rural residential buildings in the hilly terrains of Hunan Province are summarized. This work provides a specific reference for the physical model setup, and also enables to use the simulation results to provide more referential value for the location design of rural buildings in these regions. 3) The research methodology in this study is based on a combination of both wind tunnel experiments with multi-case physical scales and CFD numerical simulations. The wind tunnel experiments not only validate the accuracy and effectiveness of the developed model, but also provide further reference for the optimization of the simulation results by obtaining the relative optimal distance between the residential buildings and hills. The findings of this paper will also provide theoretical guidance for the optimal design of natural ventilation for residential buildings in hilly terrains of China.

2. Methodology

2.1. Building information and model simplification

Hunan Province, in the central China, has a humid subtropical monsoon climate. The monsoon characteristics are mainly manifested in the opposite wind directions in winter and summer, with the southerly monsoon in summer and northerly monsoon in winter (Han et al., 2009). From the perspective of improving indoor thermal environment, the buildings should be located in a way that promotes natural ventilation in summer while minimizing natural ventilation in winter to obtain reasonable natural ventilation. Through the field investigation, it is found that the planned location selection of rural modern buildings in northern Hunan Province are generally single-family buildings with scattered distribution and relatively random site selection, as shown in Fig. 1.

Table 1 shows the basic situations of some rural single-family buildings in Huarong, Pingjiang, and Liuyang countrysides in northern Hunan Province. From Table 1, it can be seen that the single-family buildings in rural areas are basically 3 bays, and a few are 2 bays or 4 bays. The width of each bay is about 4 m, and its average depth is 9.275 m. The building with 3 floors is the main building type, and a few building are 2 floors. The average height of the building is 10.37 m. The height of the windowsill is basically uniform at 0.9 m, and the height of the windows is basically 1.8 m.

Fig. 1. Rural single-family buildings in northern Hunan Province.

Considering that the residential buildings in rural areas of northern Hunan Province are mainly north-south orientation that is the main window opening direction. Therefore, in CFD simulation, the north-south wall pressure difference of building model is used as the main basis for judging the pros and cons of the location selection model. While pursuing the maximization of the north-south wall pressure difference in summer, it also considers the requirement to minimize the north-south wall pressure difference in winter. The existing location pattern of rural buildings needs to be simplified in the computer numerical simulation. The simplification of location pattern mainly includes two aspects: one is the simplification of the building body; the other is the simplification of the surrounding environment that affects natural ventilation. This study comprehensively considers the actual situation of rural buildings and the requirements of building dimension modularization for the location selection mode, as well as common settings in ventilation simulation. The rural single-family building can be simplified into a cube with a face width of 12 m (three bays), a depth of 9 m, a building height of 12 m, and a 3-story building. The specific dimensions and styles are shown in Fig. 2.

The hilly terrain of Hunan Province is low hills with continuous undulations and gentle slopes. The altitude is generally below 500 m, and the relative height does not exceed 200 m (Ying et al., 2007). This hilly terrain has no obvious veins, with a gentle slope and a rounded top, and its slope is often between 20 and 25° in Hunan Province. In geographical terms, 25° is also considered as the critical slope to distinguish between gentle hills and steep hills (Tan et al., 2021; Zhao et al., 2002). Therefore, the slope of the hills can be considered as 25° in this study. As shown in Fig. 3, the hills are simplified as a stack of layers of columns with each layer of 5 m high, and the uppermost layer has a fixed radius of 10 m (considering the roundness of the top of the hills), forming a slope of about 25°. Therefore, the floor area of the lowest layer of the hills will change accordingly with the height. Based on the survey data, two scenarios of 50 m and 150 m will be considered in the model of the location relationship between modern houses and hills in the following section. This is because when the relative height of the hills is within 200 m, the median value of the two heights can be better representative.

2.2. Basic turbulence model theory

2.2.1. Turbulence model - k-ε model

The k-ε model is currently the most widely used turbulence model in engineering problems. It was proposed by Launder and Spalding, and had been proved to be superior to various other models except for the Reynolds stress model by scholars and engineers' research and application (Zhang et al., 2020). Its turbulent energy k transport equation is given by:

$$\frac{\partial k}{\partial t}+\frac{\partial\left(\overline{u_j}k\right)}{\partial x_j}=\frac{\partial}{\partial x_j}\left(\left(\nu+\frac{\nu_t}{\sigma_k}\right)\frac{\partial k}{\partial x_j}\right)+\upsilon_i\left(\frac{\partial\overline{u_i}}{\partial x_j}+\frac{\partial\overline{u_j}}{\partial x_i}\right)\frac{\partial\overline{u_i}}{\partial x_j}-\varepsilon-2C_5\nu\left(\frac{\partial\sqrt{k}}{\partial x_i}\right)^2 \tag{1}$$

The turbulent energy viscous dissipation rate ε transport equation is:

$$\frac{\partial\varepsilon}{\partial t}+\frac{\partial\left(\overline{u_j}\varepsilon\right)}{\partial x_j}=\frac{\partial}{\partial x_j}\left(\Gamma_{seff}\frac{\partial\varepsilon}{\partial x_j}\right)+C_1f_1\frac{\varepsilon}{k}\nu_t\frac{\partial\overline{u_i}}{\partial x_j}\left(\frac{\partial\overline{u_i}}{\partial x_j}+\frac{\partial\overline{u_j}}{\partial x_i}\right)\frac{\partial\overline{u_i}}{\partial x_j}-C_2f_2\frac{\varepsilon^2}{k}$$
$$+2C_4\nu\nu_t\left(\frac{\partial^2\overline{u_i}}{\partial x_i\partial x_j}\right)^2 \tag{2}$$

Table 1
Basic situations of rural single-family buildings in northern Hunan Province.

S/N	Location	Number of floors	Floor height (m)	Total height (m)	Sill height (m)	Window height (m)	Width (m)	Depth (m)	Bay
1	Huarong	3	3.9/3.6/3.6	11.1	0.9	1.8	12	9	3
2	Huarong	3	3.9/3.8/3.8	11.5	0.9	1.8	17	9.6	4
3	Huarong	2	3.9/3.6	7.5	0.9	1.8	16	9	4
4	Huarong	3	3.8/3.6/3.6	11	0.9	1.8	11.7	8	3
5	Huarong	3	3.6/3.3/3.3	10.2	0.9	1.8	11.6	9	3
6	Huarong	3	3.9/3.6/3.6	11.1	0.9	1.8	12.1	11	3
7	Pingjiang	3	3.6/3.3/3.3	10.2	0.9	1.8	8.5	9.8	2
8	Pingjiang	2	3.6/3.3	6.9	0.9	1.8	12	8.4	3
9	Pingjiang	3	3.6/3.3	10.2	0.9	1.8	11.7	9	3
10	Pingjiang	3	3.9/3.3/3.3	10.5	0.9	1.8	11.8	9.2	3
11	Pingjiaing	3	3.9/3.7/3.7	11.3	0.9	1.8	12	9	3
12	Liuyang	3	3.6/3.6/3.6	10.8	0.9	1.8	16	12	4
13	Liuyang	3	3.9/3.5/3.5	10.9	0.9	1.8	12.3	8.9	3
14	Liuyang	3	3.9/3.6/3.6	11.1	0.9	1.8	12.9	8.9	3
15	Liuyang	3	3.9/3.3/3.3	10.5	0.9	1.8	12	8.6	3
16	Liuyang	3	3.9/3.6/3.6	11.1	0.9	1.8	11.6	9	3
Average		2.875	3.4/3.1/3.5	10.37	0.9	1.8	12.6	9.275	3.125

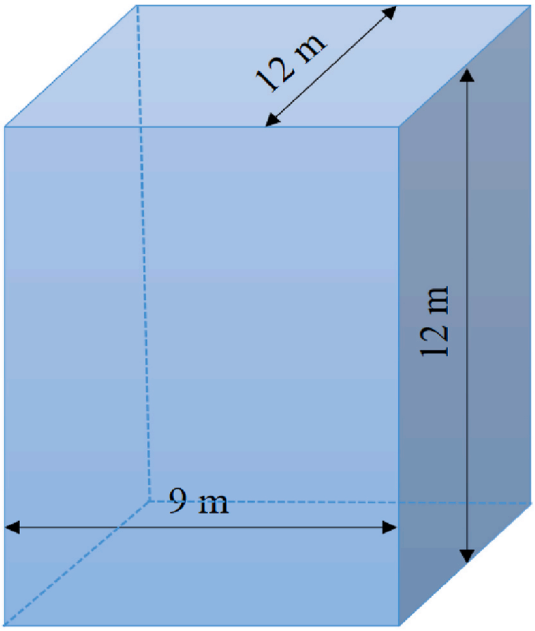

Fig. 2. Physical model of the simplified form of rural building.

Where k represents the turbulent energy; ε represents the turbulent energy viscous dissipation rate; $\overline{u_i}$ and $\overline{u_j}$ represent the velocity component in i and j direction. ν represents the kinetic energy viscosity; ν_t represents the turbulent kinetic energy viscosity coefficient; t represents the flow time; x_i and x_j represent Cartesian co-ordinates in i and j direction; Γ_{seff} represents the effective diffusion coefficient for turbulent energy dissipation rate. C_1, C_2, C_4, C_5, f_1, f_2, and σ_k are the constants in the standard k-ε model, the corresponding values can be seen in Table 2. The standard k-ε model (high R_e number turbulence model) is applied to the fully developed turbulent region at a certain distance away from the solid wall surface. In the high R_e region, ν can be ignored relative to ν_t. The solid wall boundary conditions for turbulent kinetic energy and turbulent dissipation rate are taken as the first type ($k_s = 0.0$) and the second type $\left.\frac{\partial \varepsilon}{\partial n}\right|_s = 0$, respectively.

2.2.2. Dimensionless of governing equations

For the convenience of calculation, the equations need to be dimensionless first before discretizing the differential equations with the selected qualitative velocity U_0 and qualitative length L_0. In order to facilitate the study, only the steady incompressible fluid motion is discussed. The equations after dimensionless are:

Conservation of quality:

$$\frac{\partial U_i}{\partial X_i} = 0 \tag{3}$$

Conservation of momentum:

$$\frac{\partial \left(U_i U_j\right)}{\partial X_i} = -\frac{\partial P}{\partial X_i} + \frac{\partial}{\partial X_i}\left[\left(\frac{1}{R_e} + \nu_t\right)\frac{\partial U_i}{\partial X_i} - \frac{2}{3}K\right] \tag{4}$$

Where U_i and U_j represent the dimensionless velocity component in the i and j direction; X_i represents the Cartesian coordinates of the i-direction after dimensionless; P represents the average shear stress after dimensionless; R_e represents the Reynolds number after dimensionless; K represents the turbulent kinetic energy after dimensionless.

Turbulent kinetic energy transport equation:

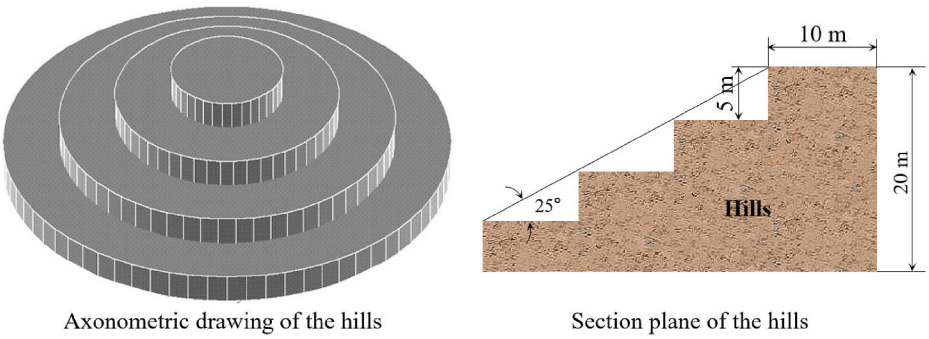

Axonometric drawing of the hills Section plane of the hills

Fig. 3. Physical model of the simplified form of the hills.

Table 2
Model constants for the standard k-ε model.

Model	σ_μ	σ_k	σ_ε	σ_T	σ_C	f_1	f_2	f_μ	C_4	C_5	C_1	C_2
Standard k-ε model	0.09	1.00	1.30	0.90	1.00	1.00	1.00	1.00	0.00	0.00	1.44	1.92

$$\frac{\partial(U_iK)}{\partial X_i}=\frac{\partial}{\partial X_i}\left(\left(\frac{1}{R_e}+\frac{v_t}{\sigma_k}\right)\frac{\partial K}{\partial X_i}\right)+P-E \tag{5}$$

Turbulent energy dissipation transport equation:

$$\frac{\partial(U_iE)}{\partial X_i}=\frac{\partial}{\partial X_i}\left(\left(\frac{1}{R_e}+\frac{v_t}{\sigma_s}\right)\frac{\partial E}{\partial X_i}\right)+C_1f_1\frac{E}{K}P-C_2f_2\frac{E^2}{K} \tag{6}$$

Average shear stress generation term in equation (4): $P = v_t\frac{\partial U_i}{\partial X_j}\left(\frac{\partial U_i}{\partial X_j}+\frac{\partial U_j}{\partial X_i}\right)$,

The turbulent kinetic energy viscosity coefficient v_t is calculated by equation (7):

$$v_t=C_\mu f_\mu\frac{K^2}{E} \tag{7}$$

Where E represents turbulent energy viscous dissipation rate after dimensionless; C_μ represents the coefficients in approximated turbulent transport equations.

The dimensionless quantity in equations (3)–(6) is defined according to equation (8):

$$X_i=\frac{x_i}{L_0}\ U_i=\frac{u_i}{U_0}\ P=\frac{p}{\rho U_0^2}\ K=\frac{k}{U_0^2}\ E=\frac{\varepsilon L_0}{U_0^3} \tag{8}$$

The dimensionless control parameters of the corresponding equations are defined by equation (9):

$$R_e=U_0L_0/v \tag{9}$$

Some related coefficients (e.g. σ_ε, f_1, f_μ, C_1 and C_2) are selected according to Table 2.

2.3. Boundary conditions and solution methods

2.3.1. Boundary conditions

(1) Incoming flow boundary conditions

The incoming flow boundary conditions are mainly to determine the distribution curve of incoming flow wind speed that is also known as the average wind speed gradient, which is the variation law of the average wind speed along the height. The wind profiles under different sites can be sorted out based on multiple observations, and proposed that the law of the average wind speed changing along the height, which can be described by an exponential function:

$$\frac{U_Z}{U_0}=\left(\frac{Z}{Z_0}\right)^a \tag{10}$$

U_Z represents the average wind speed in horizontal direction under standard reference height; Z represents the standard reference height; Z_0 represents the any height; U_0 represents the average wind speed in the horizontal direction at any height; α represents the ground roughness index.

In many literatures, the ground roughness index of rural areas is recommended to be 0.125–0.167 or 0.16 in China (Huang et al., 2008; Zhang et al., 2020). The Chinese standard also divides the ground roughness into four categories: A, B, C, and D. The category B is for fields, villages, jungles, hills, and towns and suburban areas where houses are relatively sparse, and the suggested index is 0.16 (Zhang and Zhang, 2001). Therefore, in the numerical simulation, the ground roughness index is set as 0.16. For the determination of wind speed in meteorological parameters, the wind speed at 10–12 m above the ground is taken, and the annual average wind speed in the vast majority of Hunan Province is 2–3 m/s (Han et al., 2009). Therefore, the standard reference height and average wind speed in equation (10) can be defined as the average wind speed of 3 m/s at a height of 10 m, and used as the calculation basis for numerical simulation in this study.

(2) Outflow surface boundary conditions

It is assumed that the flow on the outflow surface has been fully developed, i.e., the normal gradient of each variable is zero. This assumption can be adopted only when there is a straight section in the outflow region, and it is far away from the recirculation area. And it makes the coefficient of the corresponding direction in the discrete equation of the control volume adjacent to the boundary zero (or the downwind direction of the calculation area is large enough). For higher cases such as mountains, the assumption of local unidirectional is not strictly valid, but only an approximate treatment. The reason is that the air will generate vortices after passing through high-rise buildings or mountains, which will cause false phenomena of diffusion in a large area. Therefore, the Neumann boundary conditions are desirable. However, if the actual calculation area is large enough, the outflow wind speed can also be determined according to the conservation of mass, i.e., the Dirichlet boundary condition is adopted.

(3) Upper air surface boundary conditions

The upper air surface, like the incoming and outgoing flow surface, has no actual physical boundary and needs to make assumptions about the boundary conditions. If the computational control area is too big, the upper air surface is far from the wall of the building (or natural landform), and the incoming flow is in the horizontal wind direction. The gradient of velocity along the tangential direction can be considered as zero, and the value along the normal direction is zero. Other scalars quantities such as turbulent kinetic energy is taken as the gradient of the normal direction is zero. Upper air surface: $V = 0$, φ {U, K, ε} is the free slip condition, and the corresponding control coefficient of the pressure correction equation is zero.

(4) Near-surface boundary conditions

Near the solid wall surface, the k-ε model must be modified due to the intensified influence of laminar flow viscosity. Therefore, the solid wall boundary conditions of turbulent kinetic energy and turbulent dissipation rate are taken as the first type ($k_s = 0.0$) and the second type ($\left(\frac{\partial\varepsilon}{\partial n}\right|_s = 0$), respectively (Peng et al., 2017). The momentum on the solid wall is taken to be zero, i.e., $\varphi\{U, V\} = 0$, and the corresponding control coefficients of the pressure correction equation are zero.

(5) Treatment of the solid part of the calculation area (buildings and surrounding natural land-forms)

In the field of CFD, it is common to use methods such as the porosity method, the isolated volume method (controlling the viscosity coefficient method, using a large source term) (Tominaga and Stathopoulos, 2013). This calculation example is chosen to increase the large source term method to implement the calculation for the solid buildings and

natural features in the region, i.e., the buildings and natural features in the flow region are regarded as the overall solution algorithm of the flow.

2.3.2. Solution method

In this paper, the fluid mechanics software Fluent is used for calculation, and the finite volume method is used for the solution. The pressure-velocity correction algorithm (simple algorithm) is used, and the equations are solved iteratively. The total cycle is controlled by the mass equation residual indicator and the difference between the two iterations before and after each discrete equation.

$$\left|\left(\frac{\partial u}{\partial x}+\frac{\partial v}{\partial y}\right)_{i,j}\right|_{\max} < \varepsilon_1 \tag{11}$$

$$\left|\frac{\varphi_{i,j}^{n+1}-\varphi_{i,j}^{n}}{\varphi_{i,j}}\right| < \varepsilon_2 \tag{12}$$

When ε_1 and ε_2 are less than 10^{-5} and 10^{-4} respectively, the convergent solution will be obtained.

3. Experimental testing and model validation

To verify the correctness of the simulation, a series of wind tunnel experiments are conducted in this study with a representative rural buildings siting model in hilly terrains. The wind tunnel simulation experiments are not restricted by weather conditions, the experimental conditions (scenarios) are controllable, and it has the characteristics of short experimental period and direct observation through simulation. The experimental results are contrasted against the field observations and numerical simulations, which can provide a basis for further scientific decision-making.

3.1. Experimental instruments and equipment

3.1.1. Boundary layer wind tunnel

The wind tunnel tests were conducted in a large boundary layer of wind tunnel at Hunan University, which is one of the advanced multi-functional boundary layer wind tunnels in China (Hui et al., 2019; Li and Li, 2016; Yang et al., 2020). The aerodynamic profile of the wind tunnel is 53 m long and 18 m wide. It is a boundary layer wind tunnel with low speed, single reflow, and parallel double test sections. The first test section (high-speed test section) is 17 m long, with a model test area of 3 m wide and 2.5 m high in cross-section. The second test section (low-speed test section) is 15 m long, with a cross-sectional width of 5.5 m and a height of 4.4 m. The wind tunnel air speed control, data acquisition, and test monitoring are all concentrated in the main control room to realize fully automated computer system control, as shown in Fig. 4 and Fig. 5. The situation of the model in the wind tunnel can be monitored in real-time through the display in the control room during the wind tunnel test. The system has the function of automatic alarm for abnormal conditions, which provides an effective guarantee for the completion of high-quality wind tunnel test. The main performance of this system includes: i) steady wind control system with motor power of 619 kW, maximum wind speed of 58 m/s (Note that 58 m/s is only the maximum theoretical wind speed that this device can reach, not the actual wind speed), wind speed control accuracy of 0.3%, and wind pressure control accuracy of 0.2%; ii) turntable control system with rotational speed of 0.2 rev/min, rotational angle range of ±180°, control accuracy of ±0.1°; iii) temperature and pressure measurement system with a temperature measurement range of 0–100 °C and the accuracy ±0.5 °C; iv) the pressure measurement range in the wind tunnel with 0 ~ 2000 Pa and the accuracy of ±0.5%.

3.1.2. Wind speed and pressure measurement instrument

The anemometer used in this experiment is a Cobra pulsation wind speed tester with the type of TFI (Turbulent flow instrumentation) Series

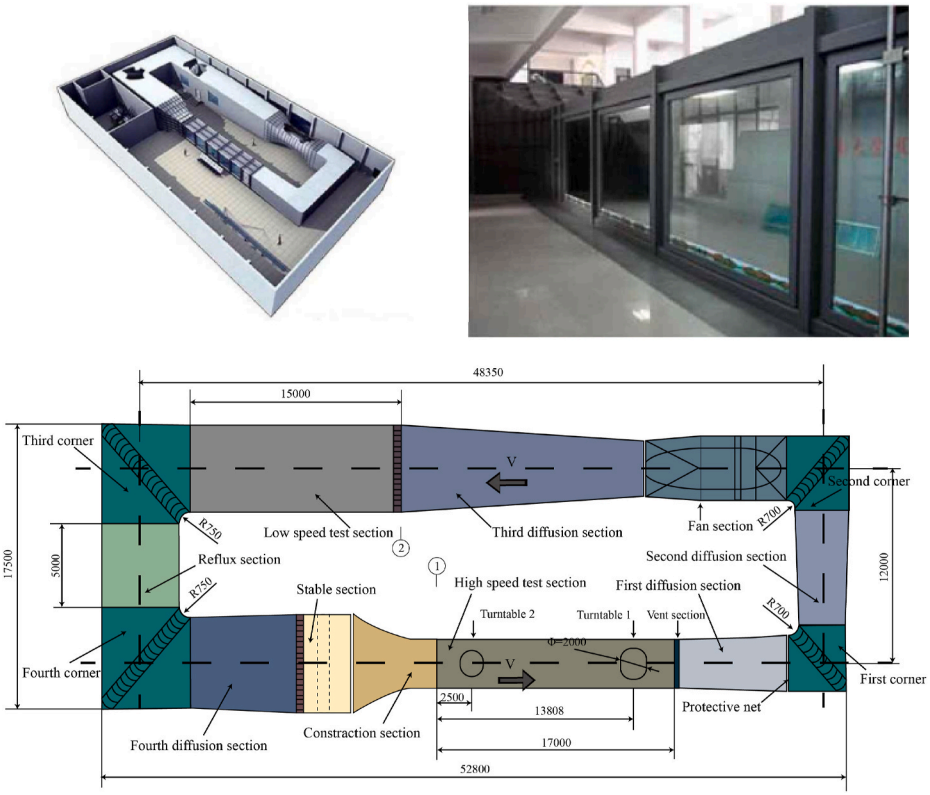

Fig. 4. Large-scale boundary layer wind tunnel and its structural layout.

Fig. 5. Wind tunnel wind speed control system.

100 Cobra Probe. The Cobra anemometer contains a 4-hole pressure probe that provides dynamic, real-time, three-vector velocity and pressure measurements. The anemometer provides a linear response frequency from 0 HZ (average flow) to 2000 HZ, and is accompanied by the TFI unit control software, which can run the anemometer and perform data acquisition. The anemometer has a range of 2–100 m/s, a deviation angle of 0–45° during measurement, and a wind speed accuracy of ±0.3 m/s. The Cobra pulsation anemometer is shown in Fig. 6 (a).

The pressure measurement instrument used in this experiment is the DTCnet electromagnetic pressure scanning valve, as shown in Fig. 6 (b). The main features of this instrument are: i) high accuracy of 0.06% for each pressure measurement channel; ii) high degree of integration with 512 channels free combination selection (64 channels/blocks × 8 blocks); iii) small size with the volume of a single 64-channel valve body of 10.7 × 4.9 × 4.3 cm; iv) multi-channel synchronous high-speed acquisition, 512-channel pressure data up to 500 HZ or more synchronous acquisition. All pressure data in this experiment are obtained by this instrument with a scanning frequency of 330 HZ and more than 18 s of continuous scanning, and a total of 6000 pressure scanning data are obtained per channel each time.

3.2. Model and measurement point distribution

The model scaling ratio in this study is 1:100, and the model includes the hilly model and building model. The hills model used in this experiment is made of expanded polystyrene board, which simulates the hills with a height of 50 m. It is formed by cutting and combining the polystyrene board as a whole. Adhesive glue is used to bond the joints, and the bonding place is smooth and flat without gaps. The specific dimensions of the hill model are shown in Fig. 7. The building model used in this experiment is assembled from plexiglass panels with pressure holes drilled on the model with a diameter of 1.2 mm. The pressure holes are distributed on the central axis of the front and back elevations of the model, arranged along the Z-axis with an axial spacing of 10 mm, and the coaxial pressure holes are equally spaced. The specific data and three-dimensional axonometric diagram of the building model are shown in Fig. 8.

The building model is fixed with bolts, and the hill model is fixed on a wooden base plate with a thickness of 10 mm with an adhesive. The base plate is then fixed on the rotating platform of the wind tunnel base plate with bolts and adhesives. The assembled model is shown in Fig. 9 (a) and (b).

In the combined model, the hills are calculated using the hills windward area due to their larger size. The projected area of the hills on the windward side is 0.55 m^2, and the size of the high-speed section of the wind tunnel is 3 × 2.5 m with an area of 7.5 m^2 as described above. Therefore, the maximum blockage ratio of this combined model is about 7.3%, which is less than the limit value of 10%, so the blockage effect is not considered in this experiment.

3.3. Boundary conditions in the experiment

3.3.1. Simulation of wind velocity distribution curves

This experiment simulates the roughness of the ground in rural areas, so that the wind tunnel airflow meets the requirements for the exponential rate of the incoming wind speed distribution curve in the above simulation, which is 0.16 as described above. To simulate the wind speed distribution curve in a wind tunnel, wedges and rough elements are required. According to the design experiences and actual investigations, the arrangement of the wedges and roughness elements in the wind tunnel is shown in Fig. 10. Before the experiment, several experimental measurements were conducted using the anemometer at different heights to validate that this arrangement could meet the requirements of gradient winds for wind tunnel tests. The vertical and horizontal spacing of the roughness elements are both 60 cm. There are 14 rows of rough elements, the first 9 rows are ordinary rough elements, and the last 5 rows are heightened rough elements. There are 3 wedges with the bottom side of 20 cm and the height of 2.5 m, and the center

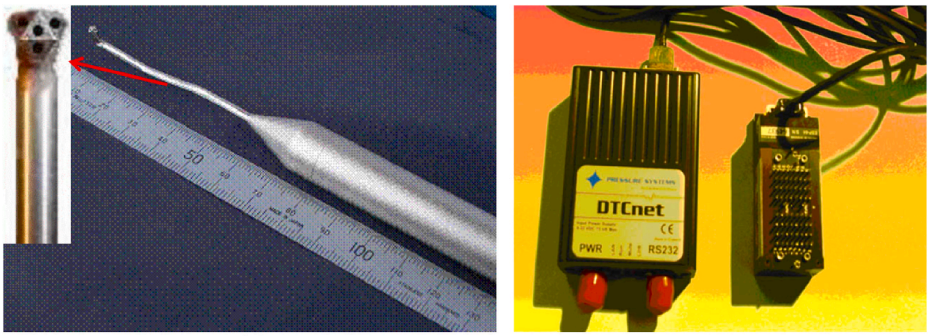

(a) (b)

Fig. 6. (a) Cobra pulsation wind speed tester; (b) DTCnet electromagnetic pressure scan valve.

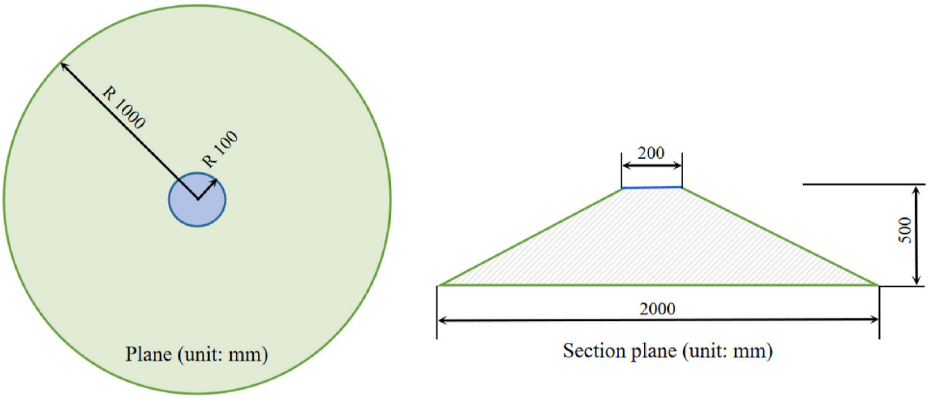

Fig. 7. Experimental model of hills.

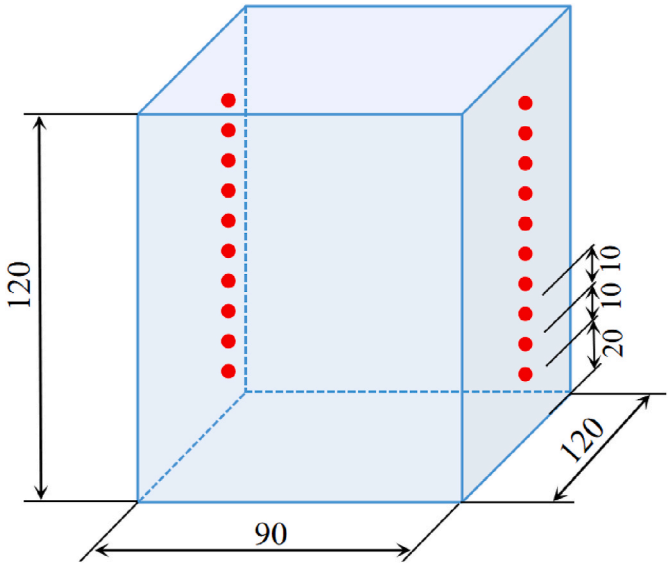

Fig. 8. Axonometric drawing of the experimental model of the building and distribution of measurement points (unit: mm).

distance between the wedges and the turntable is 10 m. The form and arrangement of the wedges and roughness elements are shown in Fig. 11.

The wind speed measurement point is selected as the center point of the wind tunnel rotating platform, which is also the location of the building model in the combined model, and the anemometer is used to test it. The measurement points are unevenly distributed along with the height: one measurement point is set every 0.02 m below 0.12 m (i.e. below the height of the building model); three measurement points are unevenly distributed between 0.12 and 0.15 m; and one measurement point is set every 0.1 m between 0.3 and 1.5 m, a total of 22 measurement points. Since the wind speed at 10 m/s is used as the benchmark in the above simulation, the actual wind speed measured at 0.1 m is also used as the benchmark in this experiment. Table 3 shows the actual wind speed, theoretical wind speed, and proportional error at each measurement point. From Table 3, it can be seen that the actual wind speed distribution curve is very consistent below 1 m, except for one measurement point, the proportional error between the remaining 17 measurement points and the theoretical value is below 3%. Considering that the building model is only 0.12 m and the hilly model is only 0.5 m, this actual wind speed distribution curve can fully meet the requirements of the experiment.

3.3.2. *Determination of experimental control wind speed*

This experiment tested the variation of wind pressure coefficients at each measurement point on the windward and leeward sides of the building model at different wind speeds. Conditions with wind speeds of 2 m/s, 4 m/s, 6 m/s, 8 m/s, 10 m/s, 12 m/s and 15 m/s were considered respectively. Figs. 12 and 13 show the results of the testing experiments. It can be seen from the figures that the wind pressure coefficients on the surface of the building model are basically the same or coincide when the control wind speed reaches or exceeds 6 m/s, and the individual measurement points are slightly different, which can be considered to be caused by experimental errors. Considering the wind tunnel operation characteristics, it takes a longer time to control the wind speed stable below 10 m/s, so the experimental control wind speed can be selected as 12 m/s. According to the Reynolds number formula of $R_e = \frac{ul}{v}$ at this time, the Reynolds number can be calculated as 7×10^4 (greater than the critical Reynolds number 10^4). It can be seen that, whether from the experimental results or the existing literature results, choosing the control wind speed of 12 m/s is reasonable to meet the experimental requirements, and also facilitate the operation control of the wind tunnel.

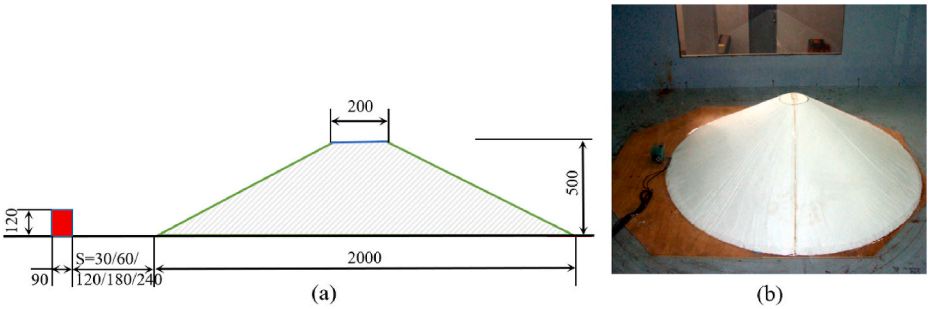

Fig. 9. Combined experimental model: (a) Side view of the combined experimental model (unit: mm); (b) Picture of Combined experimental model.

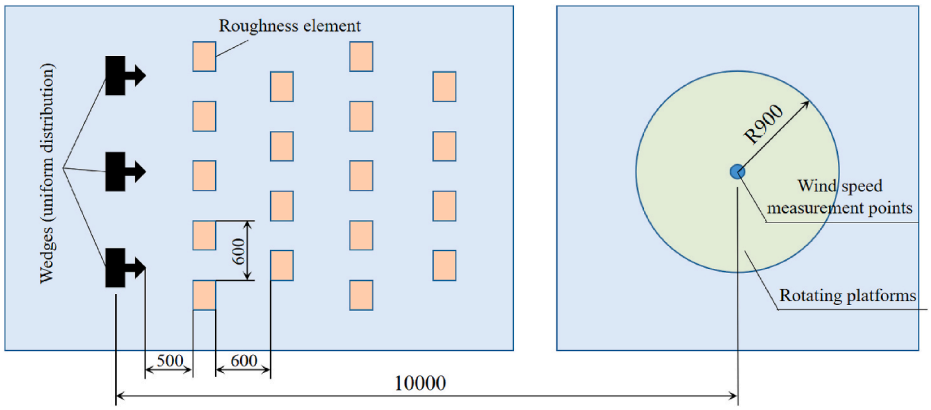

Fig. 10. Schematic diagram of wind tunnel wedges and roughness element arrangement.

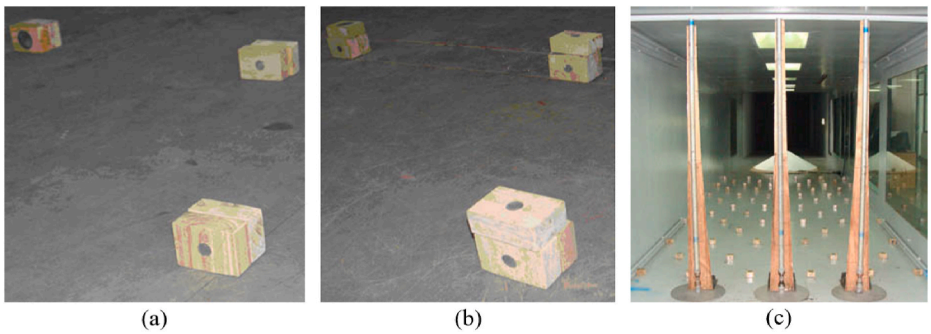

Fig. 11. Form and arrangement of roughness element and wedges: (a) Normal roughness elements; (b) Heightening roughness elements; (c) Wedges arrangement.

Table 3
Actual and theoretical values of wind speed distribution curves of wind tunnel tests.

Height (m)	Theoretical wind speed (m/s)	Actual wind speed (m/s)	Proportional error	Height (m)	Theoretical wind speed (m/s)	Actual wind speed (m/s)	Proportional error
0.02	5.25	5.62	6.61%	0.3	8.09	7.98	−1.44%
0.04	5.86	5.88	0.27%	0.4	8.48	8.51	0.40%
0.06	6.26	6.24	−0.27%	0.5	8.78	8.69	−1.08%
0.08	6.55	6.5	−0.80%	0.6	9.04	8.98	−0.72%
0.1	6.79	6.79	0.00%	0.7	9.27	9.32	0.54%
0.12	6.99	6.97	−0.30%	0.8	9.47	9.39	−0.86%
0.15	7.25	7.25	0.07%	0.9	9.65	9.68	0.31%
0.2	7.59	7.71	1.60%	1	9.81	10.1	2.83%
0.25	7.86	7.79	−0.93%				

3.4. Experimental results and analysis

The main purpose of this wind tunnel experiment is to test the surface wind pressure coefficient of the building model, and compare it with the simulation results of the building combined with the hilly site selection model below to verify the correctness of the model results and the effectiveness of the simulation method. The scaling ratio between the model and the real model is 1:100. When the building model is at the upwind, the incoming flow angle of θ is 0, which corresponds to the summer condition in the simulation below. When the building model is at the downwind, the incoming flow angle of θ is 90°, which corresponds to the winter condition in the simulation below. In addition, the spacing between the building model and the hills model was considered, and the distances were also tested as 30 mm, 60 mm, 120 mm, 180 mm, and 240 mm, which corresponded to the distances of 3 m, 6 m, 12 m, 18 m and 24 m between the building and the hills in the simulation below. The schematic diagram of the wind tunnel experiment is shown in Fig. 14. The control wind velocity of the incoming wind tunnel is 12 m/s, which is a uniform incoming flow at this time, and the gradient wind is formed at 0.1 m (corresponding to the height of 10 m in the simulation below) with a wind velocity of 9.16 m/s after the wedges and roughness element.

Figs. 15–19 show the comparison between the experimental and simulated results of wind pressure coefficient on the building surface at different intervals. Tables 4–8 show the proportional error between them. It can be seen from the figure that the trends and values of the simulation results and the experimental results are basically consistent, and the experimental results are in good agreement with the simulation results. Especially in the summer conditions (θ = 0°), the degree of agreement is more consistent than in winter conditions (θ = 90°). It can also be seen from the table that the average error of all measurement points on the same surface remains mostly within 10%, and in some cases it exceeds 10%, but the maximum is only 15.9% and the minimum is 1.20%. The proportional error of a single measurement point is mostly kept within 10%, a small part is between 10% and 20%, very few exceed 20%. From the perspective of practical engineering and design application, such simulation accuracy could meet with the requirements of design and evaluation process according to the previous literatures of

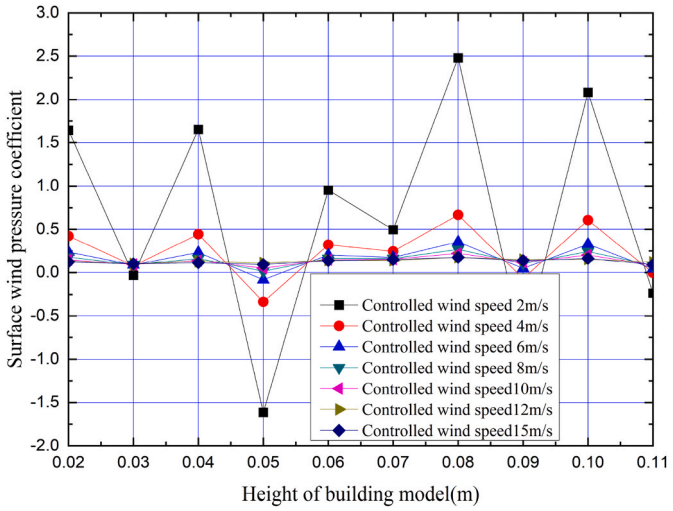

Fig. 12. Wind pressure coefficient distribution on the surface of the windward surface of the building model under different wind speeds.

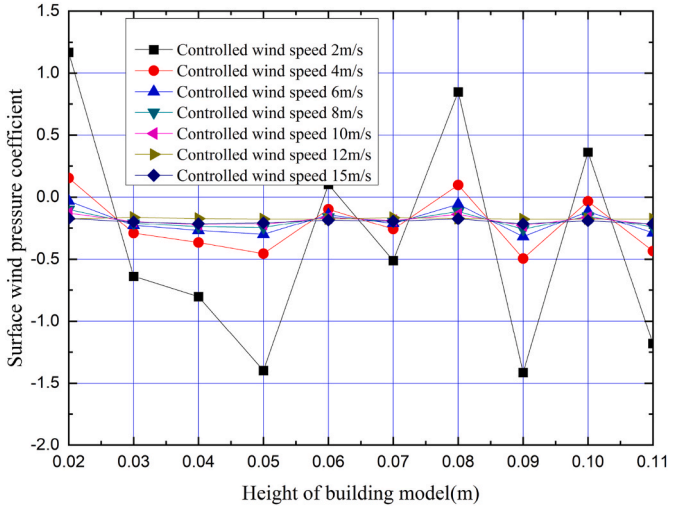

Fig. 13. Wind pressure coefficient distribution on the surface of the leeward side of the building model under different wind speeds.

natural ventilation simulation's studies (Hu et al., 2022; Kosutova et al., 2019). In addition, it can also be seen from the figures that, judging from the difference of wind pressure coefficients on the surface of both sides of the wall, the model spacing of 120 mm (i.e. the spacing between the building and the mound is 12 m in practical application) is also the best choice when winter and summer conditions are taken into account.

4. Results and discussions

4.1. Influence of residential siting pattern on natural ventilation under the hilly height of 50 m

4.1.1. Simulation object and physical model

This section mainly considers the effect on the natural ventilation of the building for a hilly height of 50 m. Based on the field research results, the building model can be chosen in the form of single-family houses. The siting model of the residential buildings can be represented in Fig. 20. As can be seen from the previous section, the distance between the buildings and hills is the key point that affects natural ventilation, combined with the policy requirement of the Chinese government to save land for rural residential buildings. Therefore, the range of variation of S in the figure with the simulation is determined by the height of the building, considering five cases of 0.25H, 0.5H, 1H, 1.5H, and 2H building heights.

4.1.2. Simulation results and analysis

Fig. 21 and Fig. 22 show the simulation results for the siting selection model of modern rural residential buildings using hills (3 m spacing), respectively. The pressure distribution diagram, the flow line diagram, the velocity vector distribution diagram, and the pressure distribution along with the height of the north and south side walls are represented in the figures, respectively. It can be seen from Fig. 21, in summer, the south wall of the building is the windward side and shows positive pressure. And the north wall is the leeward side and shows obvious negative pressure. The maximum dimensionless pressure between the north and south walls can reach up to about 0.55. The windward side of the hills has an obvious blocking effect on the airflow and forms a vortex, but it has little effect on the pressure of the north wall and has a limited effect on the natural ventilation of the building in summer. In winter, the building is located on the leeward side of the hills and is obliterated by the negative pressure, because the height of the hills is much larger than that of the building. And the dimensionless pressure between the north and south side of the wall is drastically reduced to a maximum of 0.28. The natural ventilation effect caused by the wind pressure is significantly weaker than that in summer. As can be seen from Fig. 22, the most appropriate basis for judging the natural ventilation potential of the building in winter and summer is the pressure

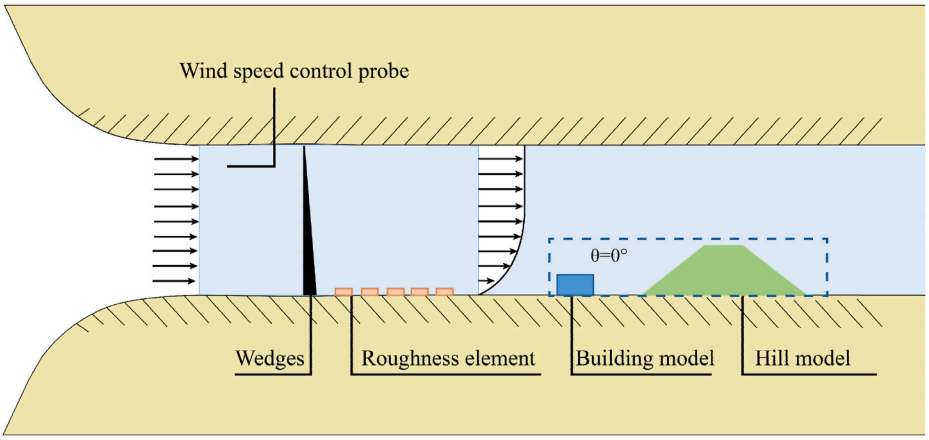

Fig. 14. Schematic diagram of wind tunnel testing.

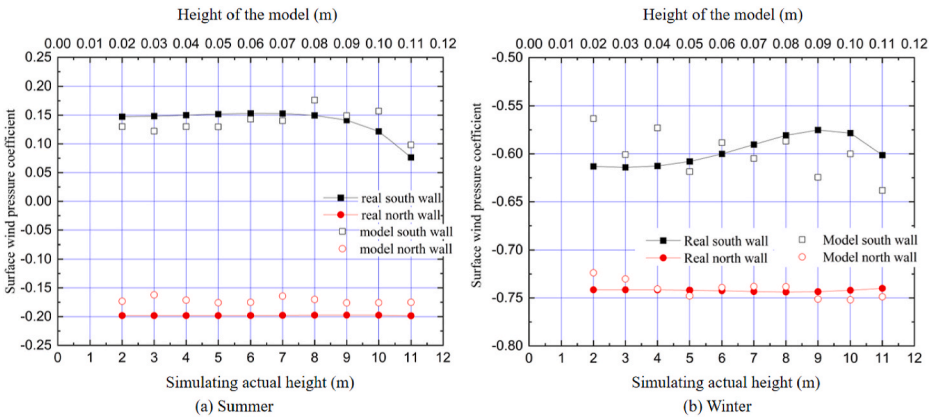

Fig. 15. Comparison of experimental results of wind pressure coefficient on building surface and simulation results (model spacing is 30 mm).

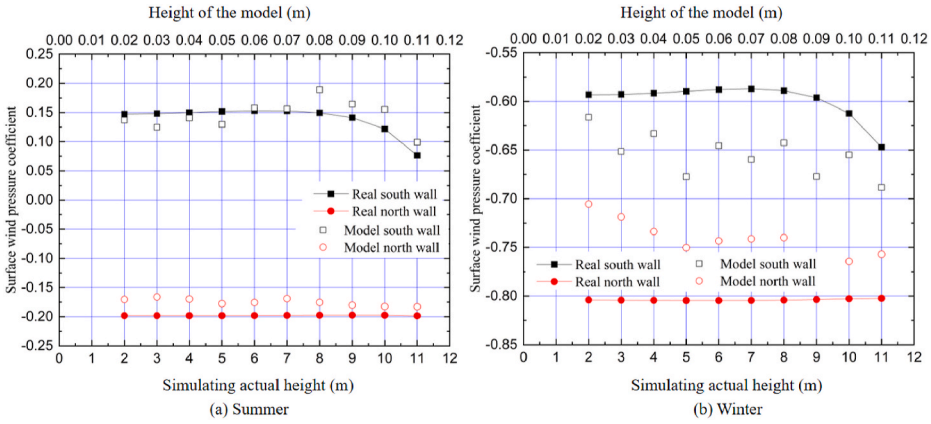

Fig. 16. Comparison between experimental results and simulation results of wind pressure coefficient on building surface (model space is 60 mm).

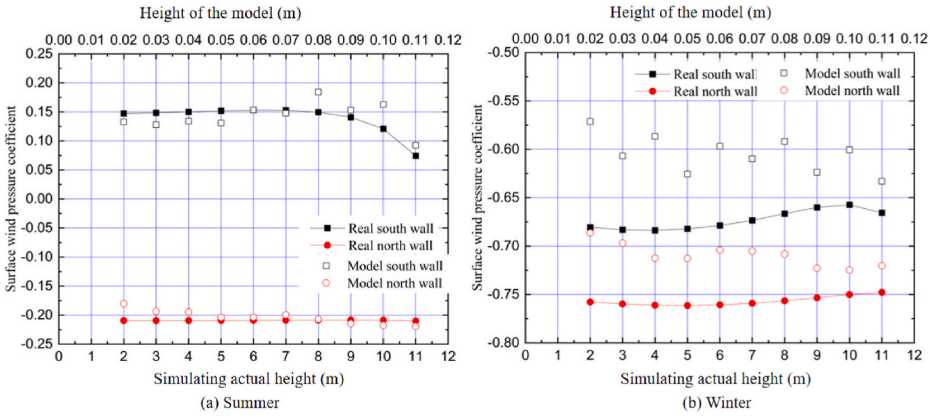

Fig. 17. Comparison between experimental results and simulation results of wind pressure coefficient on building surface (model spacing is 120 mm).

distribution along with the height of the north and south side walls of the building, which can be effectively judged by the dimensionless pressure, given the significant shading effect of the hills in winter. Therefore, in the rest of the following cases, only the pressure distribution map along the height of the north and south side walls at different distances will be used as the basis for judgment and optimization.

Considering that between 1 and 11 m at north-south side wall is mainly the position of a window opening. Therefore, the analysis of the pressure difference between the north and south side walls of the dwelling should also focus on the position of height 1–11 m. It can be seen from Figs. 23–26 that the pressure difference between the north and south side of the building increases slightly in summer with the change of the distances. The minimum pressure difference is 0.54 when S is 3 m, and it increases gradually to a maximum of 0.6 when S becomes 24 m. The reason for this situation is that the distances between the buildings and the hills gradually expand, and the influence of the hills on the buildings in the flow field gradually decreases. The vortex formed on the windward side of the hills has an impact on the north side of the building. The influence of the vortex on the pressure change of the north wall of the building is gradually decreasing. However, it should be noted that this change is not significant and the magnitude is small, and the effect on the natural ventilation effect in summer should be limited. In

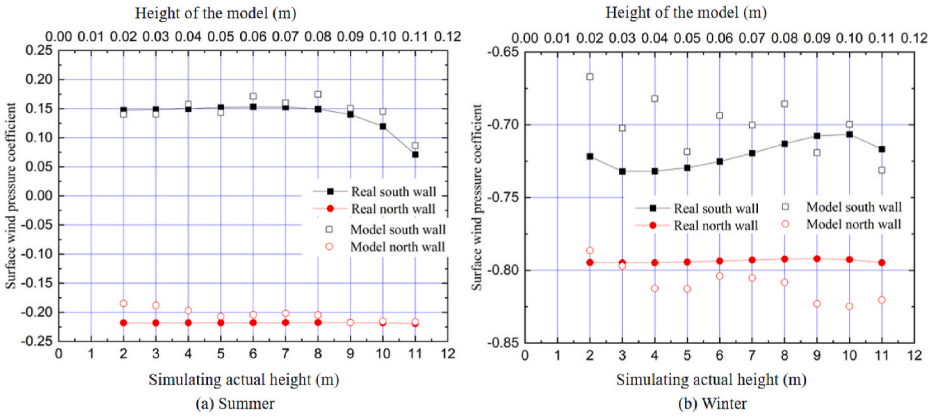

Fig. 18. Comparison between experimental results and simulation results of wind pressure coefficient on building surface (model spacing is 180 mm).

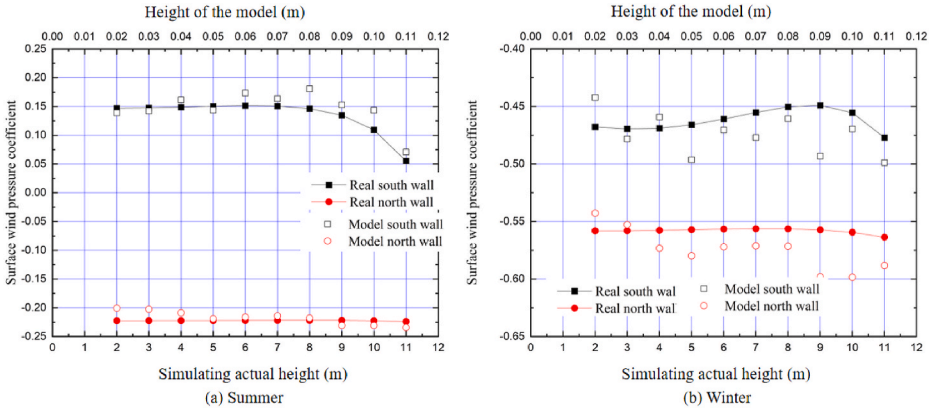

Fig. 19. Comparison between experimental results and simulation results of wind pressure coefficient on building surface (model spacing is 240 mm).

Table 4
The relative error between experimental results and simulation results of building surface wind pressure coefficient (model spacing is 30 mm).

Height of model measuring point (m)	Proportional south wall in summer	Proportional north wall in summer	Proportional south wall in winter	Proportional north wall in winter
0.02	13.33%	14.36%	8.87%	2.45%
0.03	21.38%	22.24%	2.22%	1.55%
0.04	15.30%	15.72%	6.92%	0.12%
0.05	17.04%	12.69%	−1.71%	−0.79%
0.06	6.91%	13.15%	1.99%	0.46%
0.07	8.85%	20.40%	−2.40%	0.71%
0.08	−15.04%	16.14%	−1.03%	0.74%
0.09	−5.26%	12.09%	−7.90%	−1.03%
0.10	−22.38%	12.34%	−3.63%	−1.32%
0.11	−22.09%	13.38%	−5.78%	−1.16%
Root-mean-square average	15.90%	15.61%	5.04%	1.20%

Table 5
The relative error between experimental results and simulation results of wind pressure coefficient on building surface (model spacing is 60 mm).

Height of model measuring point (m)	Proportional error of south wall in summer	Proportional error of north wall in summer	Proportional error of south wall in winter	Proportional error of north wall in winter
0.02	7.58%	16.26%	−3.77%	13.97%
0.03	18.87%	19.22%	−9.00%	11.90%
0.04	6.62%	16.76%	−6.56%	9.63%
0.05	17.14%	11.56%	−12.95%	7.23%
0.06	−3.10%	12.74%	−8.95%	8.25%
0.07	−2.23%	17.05%	−11.02%	8.54%
0.08	−20.84%	12.58%	−8.33%	8.69%
0.09	−14.01%	9.58%	−11.99%	5.54%
0.10	−21.46%	8.20%	−6.52%	5.02%
0.11	−22.71%	8.50%	−6.00%	5.98%
Root-mean-square average	15.40%	13.75%	8.94%	8.89%

winter, the maximum pressure difference between north and south is 0.26 for S = 3 m and is 0.34 for S = 6 m. Starting from S = 12 m, the maximum pressure difference between north and south side has a significant decrease, which is 0.15, 0.14, and 0.16 in order. In addition, starting from S = 12 m, the pressure difference between the north and south side between 4 m and 6 m in height is the lowest in the same condition. And between 4 m and 6 m is exactly where the windows open on the second floor of the residence, and the second floor is the floor where the bedrooms are located in the rural residence, which has the greatest impact on improving the natural ventilation of the main living rooms.

From the above analysis, it can be seen that as the distance between the building and the hills increases within a certain range, the natural ventilation potential of the building increases slightly in summer, while the potential is gradually reduced in winter. Therefore, from the perspective of simply enhancing the summer ventilation of the building and reducing the winter ventilation, when S = 2H (or 24 m) is the most worthy choice and can even be further increased, but it is not studied because it is limited to the value of the calculation range in this simulation. The farther away from the hills, the flatter the terrain, in rural

Table 6
The relative error between experimental results and simulation results of wind pressure coefficient on building surface (model spacing is 120 mm).

Height of model measuring point (m)	Proportional error of south wall in summer	Proportional error of north wall in summer	Proportional error of south wall in winter	Proportional error of north wall in winter
0.02	10.97%	16.20%	19.12%	10.39%
0.03	16.13%	8.30%	12.56%	9.02%
0.04	12.05%	7.69%	16.55%	6.84%
0.05	16.11%	2.55%	9.06%	6.82%
0.06	0.01%	2.58%	13.71%	8.04%
0.07	3.49%	4.53%	10.42%	7.63%
0.08	−18.79%	0.65%	12.58%	6.81%
0.09	−7.85%	−2.86%	5.81%	4.21%
0.10	−25.70%	−4.11%	9.43%	3.50%
0.11	−19.57%	−4.18%	5.15%	3.80%
Root-mean-square average	15.02%	6.83%	12.18%	7.04%

Table 7
The relative error between experimental results and simulation results of building surface wind pressure coefficient (model spacing is 180 mm).

Height of model measuring point (m)	Proportional error of south wall in summer	Proportional error of north wall in summer	Proportional error of south wall in winter	Proportional error of north wall in winter
0.02	4.96%	18.07%	3.71%	1.05%
0.03	5.59%	16.09%	4.25%	−0.26%
0.04	−4.82%	10.72%	7.31%	−2.18%
0.05	5.99%	5.25%	1.52%	−2.27%
0.06	−10.64%	6.70%	4.56%	−1.29%
0.07	−4.44%	7.89%	2.76%	−1.53%
0.08	−14.54%	6.39%	3.99%	−1.99%
0.09	−6.87%	−0.15%	−1.60%	−3.76%
0.10	−17.76%	1.24%	0.98%	−3.90%
0.11	−17.54%	1.31%	−1.97%	−3.12%
Root-mean-square average	10.63%	9.38%	3.73%	2.41%

Table 8
The relative error between experimental results and simulation results of wind pressure coefficient on building surface (model spacing is 240 mm).

Height of model measuring point (m)	Proportional error of south wall in summer	Proportional error of north wall in summer	Proportional error of south wall in winter	Proportional error of north wall in winter
0.02	5.74%	10.86%	5.73%	2.84%
0.03	3.66%	9.90%	−1.83%	0.95%
0.04	−7.96%	6.49%	2.10%	−2.72%
0.05	4.71%	1.51%	−6.14%	−3.91%
0.06	−12.59%	2.77%	−2.04%	−2.71%
0.07	−7.81%	3.65%	−4.56%	−2.62%
0.08	−19.11%	1.86%	−2.23%	−2.66%
0.09	−11.79%	−3.80%	−8.95%	−6.82%
0.10	−23.84%	−3.63%	−3.01%	−6.53%
0.11	−22.15%	−4.46%	−4.37%	−4.18%
Root-mean-square average	13.84%	5.76%	4.65%	3.99%

areas are often farmland. Whether the Ministry of Construction's requirement of "energy-saving and land-saving" greenhouses or the Ministry of Land and Resources' requirement of "protecting basic farmland" restricts the siting of rural buildings from encroaching too much on farmland, and it would be more appropriate to use slopes and hills. Therefore, combined with the simulation results above, it can be considered that the distance between the building and the hills is the best value of S = 1H = 12 m, which not only takes into account the different requirements for natural ventilation of rural buildings in winter and summer but also conforms to the scientific experience extracted from traditional residential buildings and meets the national call for land-saving rural regions.

4.2. Influence of residential siting selection pattern on natural ventilation at a hilly height of 150 m

4.2.1. Physical model

Based on the above method, in the case that the height of the hills is 150 m, the building and hills can be simplified as shown in Fig. 27, and their profiles are used as the basis of computer numerical simulation. However, due to the large hills, when the distance between the buildings and the hills is too small, the change of the result is also very small, which is not conducive to analysis and selection optimization. Therefore, in the calculation example of hills with a height of 150 m, the distance between buildings and hills considered in this study varies among 0.5H, 1H, 5H, and 10H (H is the building height).

4.2.2. Simulation results and analysis

In this section, the distribution of surface pressure along the wall height on the north and south side of the building is still used for analysis and optimization. At the same time, due to the expansion of the distance between the building and hills, the change and interaction of the flow field between the hills and building gradually increase its influence on the building, which is also a factor that need to be considered. Therefore, the flow field vector diagrams under different conditions are also put into the simulation results in order to facilitate the discussion.

As can be seen from Figs. 28–31, in summer, the pressure on the north wall starts to increase when the height of the hills increases to 150 m, compared to the case when the height of the hills is 50 m, which is basically a positive value. It is only when the distance is enlarged to 120 m, it will be displayed as a negative value. This indicates that when the height of the hills increases, the obstructive effect of the windward face of the hills on the flow field increases. And the vortex formed by the deflected airflow has an obvious influence on the pressure distribution on the north wall. As the distance between the hills and the buildings increases, this effect starts to decrease gradually. The dimensionless pressure on the north wall gradually decreases from 0.14 at S = 6 m to −0.02 at S = 120 m. The obstructive effect of hills in summer is also reflected in the pressure difference between the north and south walls. Since the south wall is the windward side, the dimensionless pressure is basically unchanged. With the gradual decrease of the dimensionless pressure on the north wall caused by the expansion of the distance, the dimensionless pressure difference between the north and the south walls increases from 0.18 at S = 3 m to 0.34 at S = 120 m. It can be seen that the difference of the dimensionless pressure on the north and south walls is much smaller than 0.54 at a distance of 12 m between the building and the hills at a height of 150 m, even if the distance between the building and the hills reaches 120 m. It can be concluded that the height of the hills has a proportional effect on the summer ventilation of the building, and the hills selected for the building site should be carefully considered. In winter, it can be seen from the flow field vector diagram that the airflow is relatively more complex and variable on the leeward side of the hills after being blocked by the hills, and the negative pressure on the south wall is even greater than that on the north wall at S = 12 m. In terms of ventilation potential alone, it is possible to analyze the dimensionless pressure on both sides. It can be seen that the dimensionless pressure is 0.19 at S = 6 m, 0.1 at S = 12 m, maximum 1.06 at S = 60 m, and 0.06 at S = 120 m. In terms of the seasonal requirements for natural ventilation, the distance between the building and the hills is optimal at S = 120 m in this case. However, considering the land-saving requirement of building site selection, the second-best choice of S = 12 m is more suitable for the actual situation in rural areas of Hunan Province. Although this will lose some natural ventilation potential in

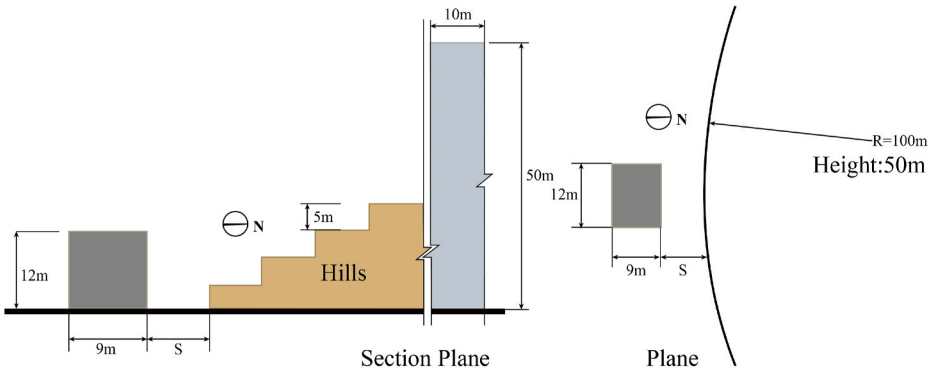

Fig. 20. Physical model of single-family house combined with hilly site selection model (Hill height = 50 m).

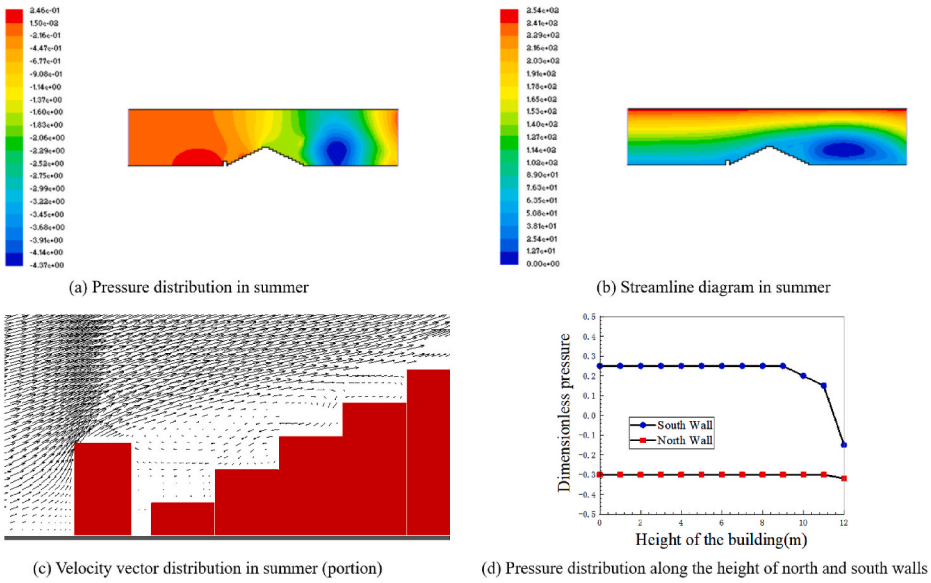

Fig. 21. Simulation results of natural ventilation for residential buildings in summer (S = 0.25H = 3 m; Hill height = 50 m).

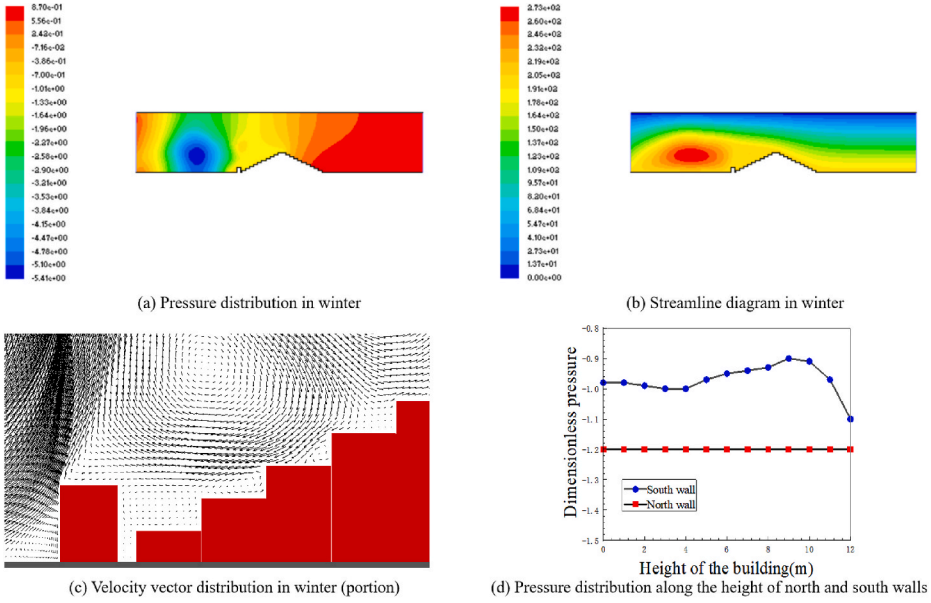

Fig. 22. Simulation results of natural ventilation for residential buildings in winter (S = 0.25H = 3 m; Hill height = 50 m).

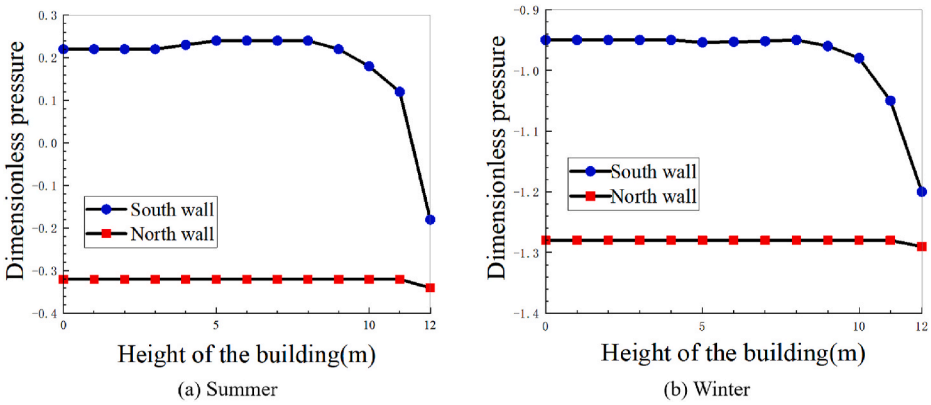

Fig. 23. Pressure distribution along the height of the wall on the north and south sides of the residence (S = 0.5H = 6 m; Hill height = 50 m).

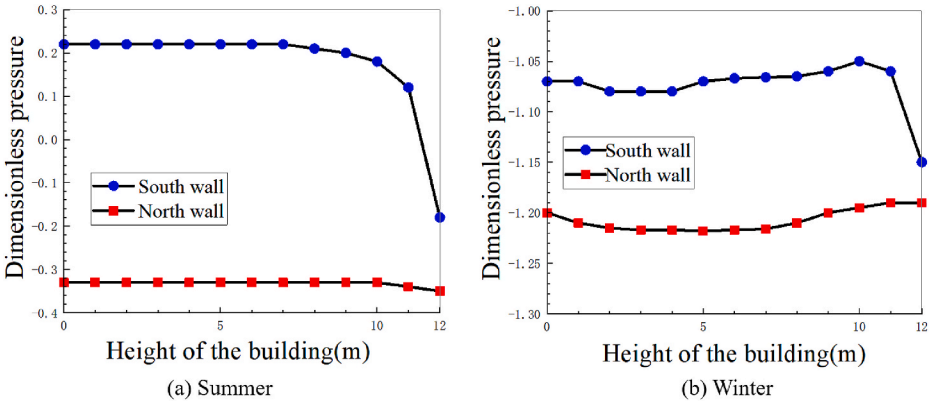

Fig. 24. Pressure distribution along the height of the wall on the north and south sides of the residence (S = 1H = 12 m; Hill height = 50 m).

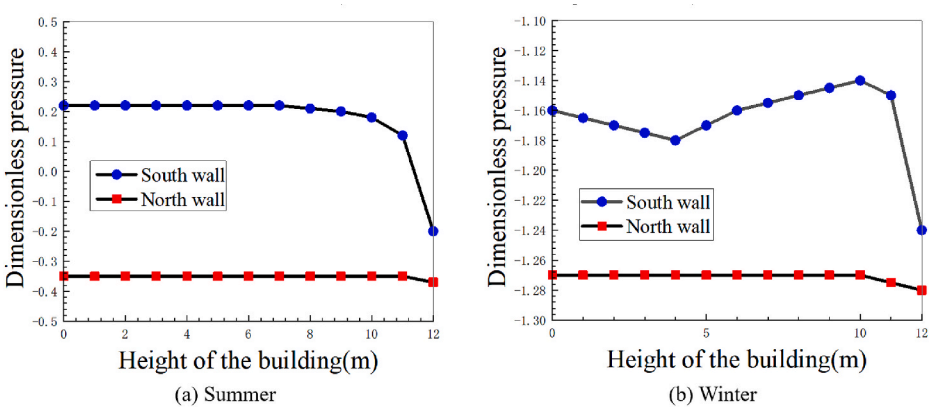

Fig. 25. Pressure distribution along the height of the wall on the north and south sides of the residence (S = 1.5H = 18 m; Hill height = 50 m).

summer, it is more beneficial for reducing natural ventilation and strengthening indoor heat preservation in winter.

4.3. The optimal site selection mode of single-family residential buildings combined with hills

There are many requirements for the site selection of residential buildings in rural hilly areas of Hunan Province. On the one hand, it is necessary to use hills to seek advantages and avoid disadvantages, with as much natural ventilation in summer as possible, while minimizing natural ventilation in winter. On the other hand, considering the current situation of large population and small land in the rural areas of Hunan Province, it is necessary to reduce the encroachment on farmland as much as possible, and to make use of the gently sloping land near the root of the hills. This is also consistent with the requirement of "energy-saving and land-saving green housing" proposed by the Chinese government. In this section, the CFD method is used to simulate the potential of building ventilation in winter and summer under different hilly heights. The results show that the impact on the natural ventilation of building in summer increases as the height of the hills increases. Combining all requirements, a building distance of about 12 m from the hills is a more appropriate value under different hilly heights. It can also be seen that the results obtained from the wind tunnel experimental tests and numerical simulations are relatively consistent, which is also

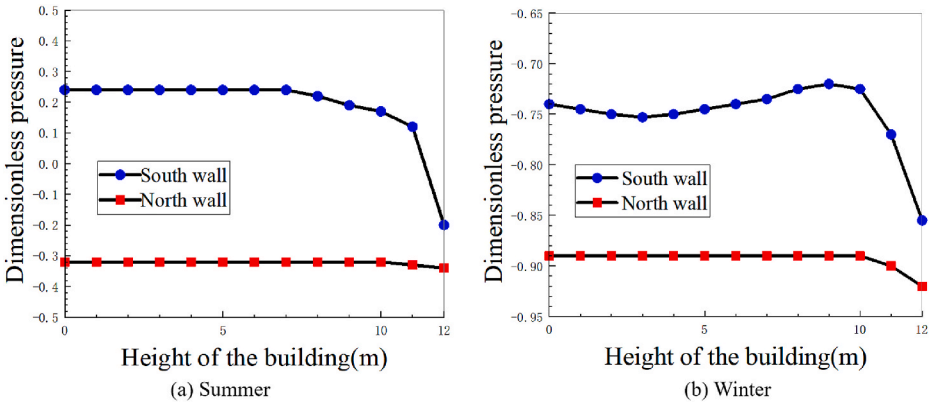

Fig. 26. Pressure distribution along the height of the wall on the north and south sides of the residence (S = 2H = 24 m; Hill height = 50 m).

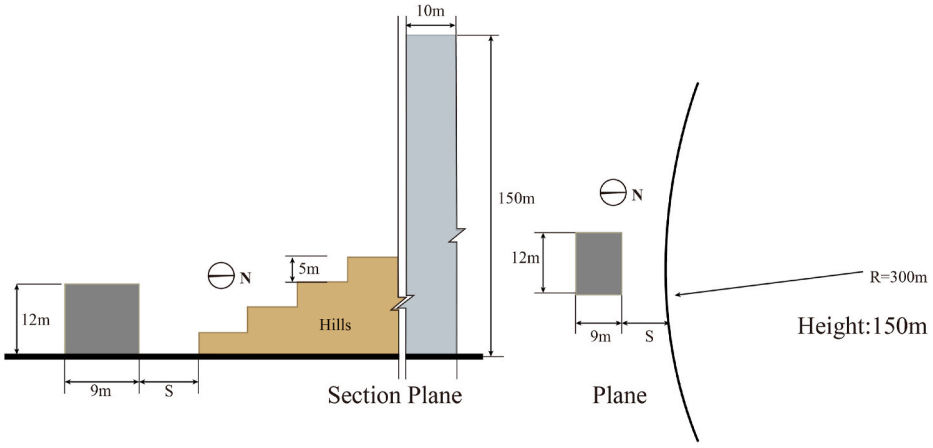

Fig. 27. Physical model of single-family residence combined with hill site selection model (Hill height = 150 m).

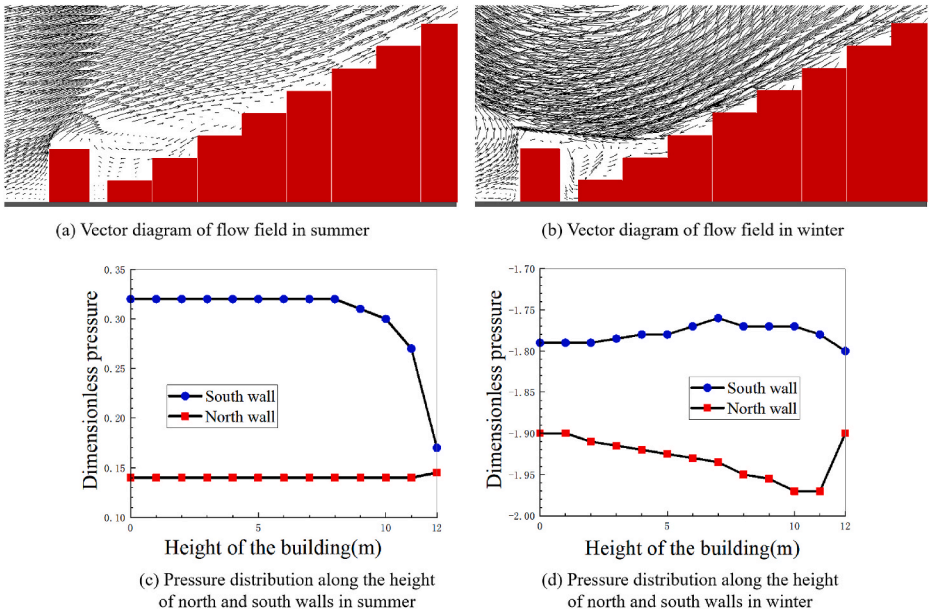

Fig. 28. Simulation results of residential natural ventilation (S = 0.5H = 6 m; Hill height = 150 m).

confirms the correctness of the 12 m value on the other hand. In this regard, the optimal model for the site location of rural single-family residential buildings combined with hills in northern Hunan Province can be obtained, as shown in Fig. 32.

5. Conclusions and future studies

Natural ventilation is one of the passive technical measures that are worthy of priority consideration in rural areas of Hunan Province from

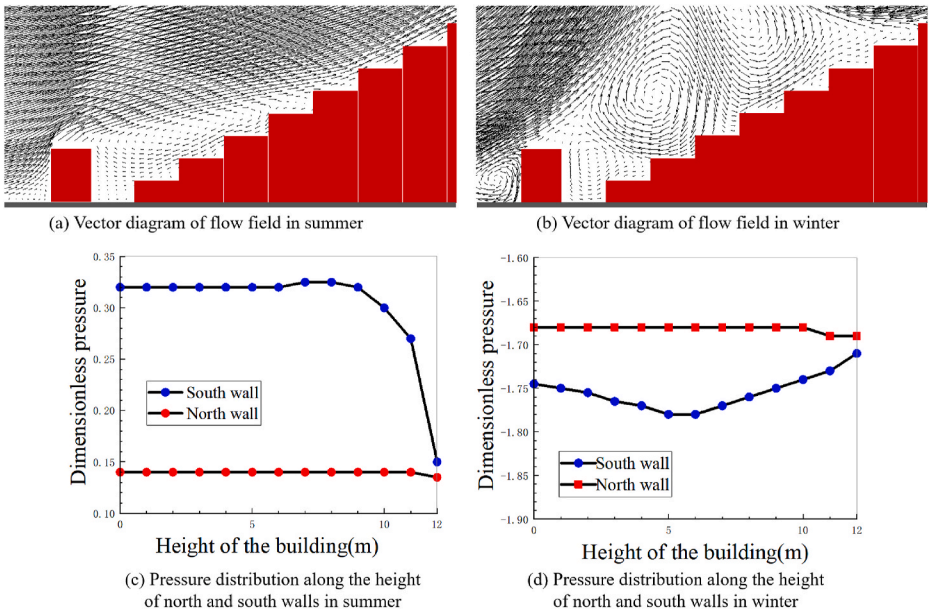

Fig. 29. Simulation results of residential natural ventilation (S = 1H = 12 m; Hill height = 150 m).

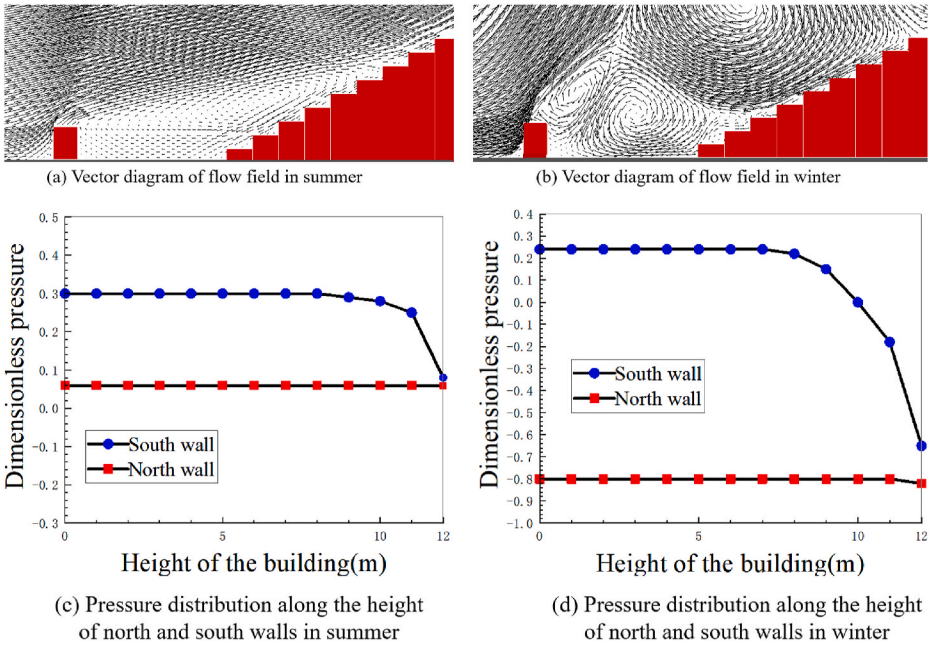

Fig. 30. Simulation results of residential natural ventilation (S = 5H = 60 m; Hill height = 150 m).

various perspectives such as energy-saving, thermal comfort, and health. This paper presents wind tunnel experiments and numerical simulations of natural ventilation in rural residential buildings in the hilly terrain of Hunan Province from the perspective of building site selection. The aim is to analyze the different site selection patterns from multiple angles thereby proposing rationalized improvement suggestions. The main conclusions of this paper can be summarized as follows.

A large amount of data research was conducted for several typical rural areas in northern Hunan Province (Huarong, Pingjiang, and Liuyang counties) to obtain a comprehensive understanding of the local residential situation. The study shows that these rural areas are generally single-family residential buildings, which are scattered and located relatively close to the hills. Based on the investigation data, the design characteristics and site location patterns of rural residential buildings are summarized, thereby providing a reference for the physically-based modelling of the simulation.

Wind tunnel experiments were carried out according to different rural residential buildings site selection patterns under hilly terrain, with a scaling ratio of 1:100 between the experimental model and the simulated real model. Five cases were tested for the distance between the building model and the hilly model of 30 mm, 60 mm, 120 mm, 180 mm, and 240 mm, corresponding to the distance between the building and the hills in the simulation of 3 m, 6 m, 12 m, 18 m, and 24 m. The study shows that the experimental results are in good agreement with the simulation results, especially the summer conditions are better than the winter conditions. The average error is basically within 10%, and most of the errors of individual measurement points are within 20%. In addition, it can also be obtained from the wind tunnel experimental data

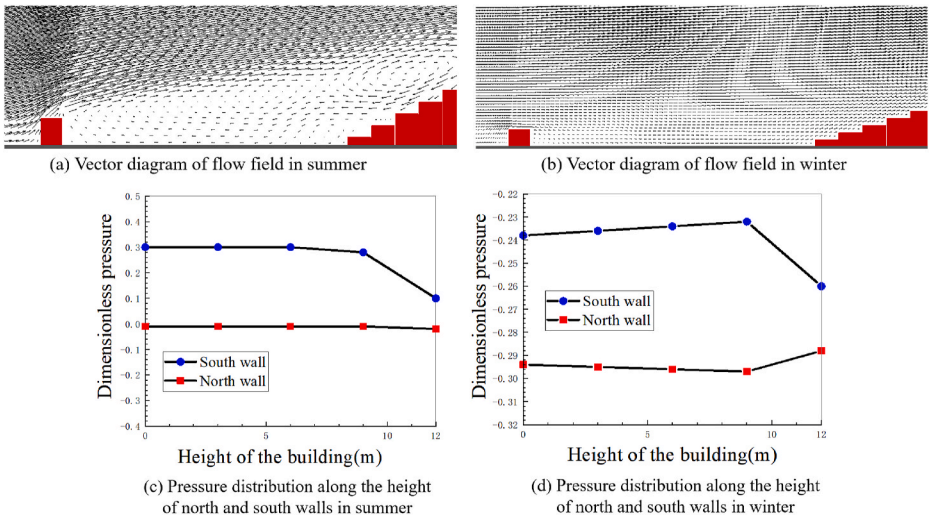

Fig. 31. Simulation results of residential natural ventilation (S = 10H = 120 m; Hill height = 150 m).

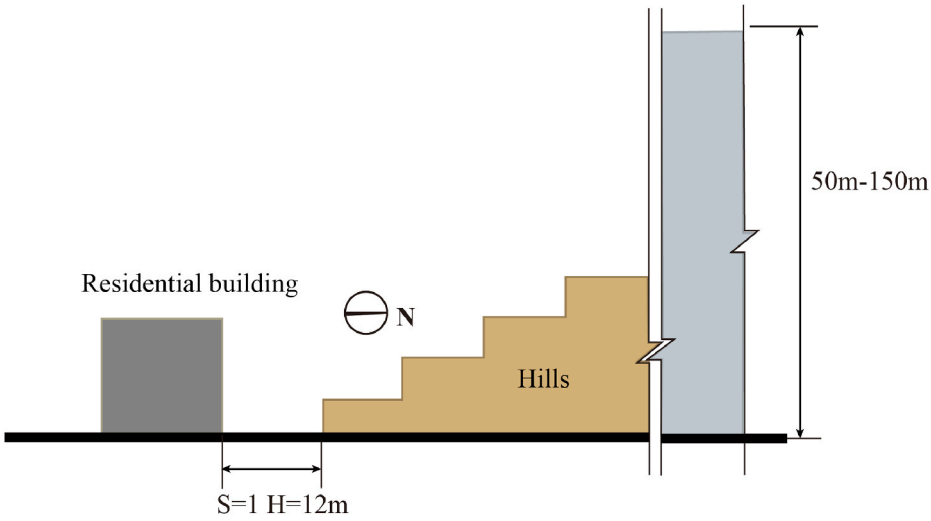

Fig. 32. The optimal site selection mode of single-family residential buildings combined with hills.

that, based on the difference of wind pressure coefficients on both sides of the wall surface, when the model spacing is 120 mm (the distance between the building and the hills is 12 m in practical application) is relatively the optimal selection considering the winter and summer conditions.

Under hilly terrains, the building ventilation in the existing model is obviously blocked in winter, which is favourable to the indoor thermal environment in winter. However, the natural ventilation is affected to some extent in summer, and the optimal distance between the building and hills needs to be investigated and selected. The results show that, in hilly terrains, regardless of whether the height of the hills is 50 m or 150 m, when the distance between the building and the heel edge of the hills is one time the building height (i.e. 12 m), the building is able to avoid natural ventilation in winter to the maximum extent while minimizing summer ventilation.

In future studies, more rural residential buildings can also be investigated nationwide to summarize more rural building design patterns, optimize and improve various patterns based on CFD simulation methods, and provide more references for the natural ventilation design of rural buildings in different regions. On the other hand, rural residential buildings are usually surrounded by green trees, which at a certain height also have a considerable influence on the natural ventilation of the buildings. Therefore, it is also essential to carry out the subsequent studies on the optimal pattern of single-family residential buildings combined with green arboriculture in selected rural regions of Hunan Province. In addition, it is also important to consider some studies on the combination design methodologies of other energy saving technologies with different typologies of rural residential buildings. These effective measures could strengthen their natural ventilation efficiency and further improve the indoor thermal comfort, e.g. tunnel ventilation, Trombe curtain wall technologies, etc.

CRediT authorship contribution statement

Mingjing Xie: Conceptualization, Investigation, Experiment, Methodology, Resources, Software, Validation, Writing – original draft. **Yuran Wang:** Investigation, Methodology, Software, Validation, Writing – original draft. **Zhengxuan Liu:** Conceptualization, Methodology, Resources, Software, Validation, Supervision, Writing – review & editing. **Guoqiang Zhang:** Supervision, Investigation, Methodology, Resources.

Declaration of competing interest

The authors declare that they have no known competing financial interests or personal relationships that could have appeared to influence the work reported in this paper.

References

Aflaki, A., Mahyuddin, N., Al-Cheikh Mahmoud, Z., Baharum, M.R., 2015. A review on natural ventilation applications through building façade components and ventilation openings in tropical climates. Energy Build. 101, 153–162.

Calama-González, C.M., Suárez, R., León-Rodríguez, Á.L., 2022. Thermal comfort prediction of the existing housing stock in southern Spain through calibrated and validated parameterized simulation models. Energy Build. 254, 111562.

Chen, Y., Tong, Z., Zheng, Y., Samuelson, H., Norford, L., 2020. Transfer learning with deep neural networks for model predictive control of HVAC and natural ventilation in smart buildings. J. Clean. Prod. 254, 119866.

Han, J., Yang, W., Zhou, J., Zhang, G., Zhang, Q., Moschandreas, D.J., 2009. A comparative analysis of urban and rural residential thermal comfort under natural ventilation environment. Energy Build. 41 (2), 139–145.

He, X., Shen, S., Miao, S., Dou, J., Zhang, Y., 2015. Quantitative detection of urban climate resources and the establishment of an urban climate map (UCMap) system in Beijing. Build. Environ. 92, 668–678.

Heiselberg, P., 2002. Principles of Hybrid Ventilation. Annex 35: Hybrid Ventilation in New and Retrofitted Office Buildings(1395-7953 R0207), pp. 1–75.

Hu, H., Kikumoto, H., Ooka, R., Lin, C., Zhang, B., 2022. Comprehensive validation of experimental and numerical natural ventilation predictions based on field measurement with experimental house. Build. Environ. 207, 108433.

Huang, B.W.C., 2008. Principles and Applications of Structural Wind Resistance Analysis, 2008. Tongji University Press, Shanghai, pp. 14–169 (In Chinese).

Hui, Y., Yuan, K., Chen, Z., Yang, Q., 2019. Characteristics of aerodynamic forces on high-rise buildings with various façade appurtenances. J. Wind Eng. Ind. Aerod. 191, 76–90.

Huo, T., Ren, H., Zhang, X., Cai, W., Feng, W., Zhou, N., Wang, X., 2018. China's energy consumption in the building sector: a Statistical Yearbook-Energy Balance Sheet based splitting method. J. Clean. Prod. 185, 665–679.

Izadyar, N., Miller, W., Rismanchi, B., Garcia-Hansen, V., 2020. Impacts of façade openings' geometry on natural ventilation and occupants' perception: a review. Build. Environ. 170, 106613.

Jomehzadeh, F., Hussen, H.M., Calautit, J.K., Nejat, P., Ferwati, M.S., 2020. Natural ventilation by windcatcher (Badgir): a review on the impacts of geometry, microclimate and macroclimate. Energy Build. 226, 110396.

Jomehzadeh, F., Nejat, P., Calautit, J.K., Yusof, M.B.M., Zaki, S.A., Hughes, B.R., Yazid, M.N.A.W.M., 2017. A review on windcatcher for passive cooling and natural ventilation in buildings, Part 1: indoor air quality and thermal comfort assessment. Renew. Sustain. Energy Rev. 70, 736–756.

Kosutova, K., van Hooff, T., Vanderwel, C., Blocken, B., Hensen, J., 2019. Cross-ventilation in a generic isolated building equipped with louvers: wind-tunnel experiments and CFD simulations. Build. Environ. 154, 263–280.

Larsen, T.S., Plesner, C., Leprince, V., Carrié, F.R., Bejder, A.K., 2018. Calculation methods for single-sided natural ventilation: now and ahead. Energy Build. 177, 279–289.

Ledo Gomis, L., Fiorentini, M., Daly, D., 2021. Potential and practical management of hybrid ventilation in buildings. Energy Build. 231, 110597.

Li, B., You, L., Zheng, M., Wang, Y., Wang, Z., 2020. Energy consumption pattern and indoor thermal environment of residential building in rural China. Energy and Built. Environ. 1 (3), 327–336.

Li, Y., Li, Q.-S., 2016. Wind-induced response based optimal design of irregular shaped tall buildings. J. Wind Eng. Ind. Aerod. 155, 197–207.

Liu, Z., Yu, Z., Yang, T., Qin, D., Li, S., Zhang, G., Haghighat, F., Joybari, M.M., 2018. A review on macro-encapsulated phase change material for building envelope applications. Build. Environ. 144, 281–294.

Lyu, W., Li, X., Shi, W., Wang, B., Huang, X., 2021. A general method to evaluate the applicability of natural energy for building cooling and heating: revised degree hours. Energy Build. 250, 111277.

Ma, L., Zhang, X., Li, D., Arıcı, M., Yıldız, Ç., Li, Q., Zhang, S., Jiang, W., 2020. Influence of sunspace on energy consumption of rural residential buildings. Sol. Energy 211, 336–344.

Meng, X., Wang, Y., Xing, X., Xu, Y., 2020. Experimental study on the performance of hybrid buoyancy-driven natural ventilation with a mechanical exhaust system in an industrial building. Energy Build. 208, 109674.

Miri, P., Babakhani, P., 2021. On the failure of the only vernacular windcatcher in the mountainous region of Western Iran: opportunities for energy-efficient buildings. J. Clean. Prod. 295, 126383.

Nomura, M., Hiyama, K., 2017. A review: natural ventilation performance of office buildings in Japan. Renew. Sustain. Energy Rev. 74, 746–754.

Omrani, S., Garcia-Hansen, V., Capra, B., Drogemuller, R., 2017. Natural ventilation in multi-storey buildings: design process and review of evaluation tools. Build. Environ. 116, 182–194.

Peng, Y., Ma, X., Zhao, F., Liu, C., Mei, S., 2017. Wind driven natural ventilation and pollutant dispersion in the dense street canyons: wind Opening Percentage and its effects. Procedia Eng. 205, 415–422.

Remion, G., Moujalled, B., El Mankibi, M., 2019. Review of tracer gas-based methods for the characterization of natural ventilation performance: comparative analysis of their accuracy. Build. Environ. 160, 106180.

Sakiyama, N.R.M., Mazzaferro, L., Carlo, J.C., Bejat, T., Garrecht, H., 2021. Natural ventilation potential from weather analyses and building simulation. Energy Build. 231, 110596.

Schulze, T., Gürlich, D., Eicker, U., 2018. Performance assessment of controlled natural ventilation for air quality control and passive cooling in existing and new office type buildings. Energy Build. 172, 265–278.

Shafiei Fini, A., Moosavi, A., 2016. Effects of "wall angularity of atrium" on "buildings natural ventilation and thermal performance" and CFD model. Energy Build. 121, 265–283.

Shan, M., Wang, P., Li, J., Yue, G., Yang, X., 2015. Energy and environment in Chinese rural buildings: situations, challenges, and intervention strategies. Build. Environ. 91, 271–282.

Stavrakakis, G.M., Zervas, P.L., Sarimveis, H., Markatos, N.C., 2010. Development of a computational tool to quantify architectural-design effects on thermal comfort in naturally ventilated rural houses. Build. Environ. 45 (1), 65–80.

Tan, J., Zuo, J., Xie, X., Ding, M., Xu, Z., Zhou, F., 2021. MLAs land cover mapping performance across varying geomorphology with Landsat OLI-8 and minimum human intervention. Ecol. Inf. 61, 101227.

Tominaga, Y., Stathopoulos, T., 2013. CFD simulation of near-field pollutant dispersion in the urban environment: a review of current modeling techniques. Atmos. Environ. 79, 716–730.

Vassella, C.C., Koch, J., Henzi, A., Jordan, A., Waeber, R., Iannaccone, R., Charrière, R., 2021. From spontaneous to strategic natural window ventilation: improving indoor air quality in Swiss schools. Int. J. Hyg Environ. Health 234, 113746.

Wu, Y., Gao, N., Niu, J., Zang, J., Cao, Q., 2021. Numerical study on natural ventilation of the wind tower: effects of combining with different window configurations in a low-rise house. Build. Environ. 188, 107450.

Yang, J., Wang, Y., Xue, B., Li, Y., Xiao, X., Xia, J., He, B., 2021. Contribution of urban ventilation to the thermal environment and urban energy demand: different climate background perspectives. Sci. Total Environ. 795, 148791.

Yang, Q., Liu, Z., Hui, Y., Li, Z., 2020. Modification of aerodynamic force characteristics on high-rise buildings with arrangement of vertical plates. J. Wind Eng. Ind. Aerod. 200, 104155.

Ying, X., Zeng, G.-M., Chen, G.-Q., Tang, L., Wang, K.-L., Huang, D.-Y., 2007. Combining AHP with GIS in synthetic evaluation of eco-environment quality—a case study of Hunan Province, China. Ecol. Model. 209 (2), 97–109.

Zhang, H., Yang, D., Tam, V.W.Y., Tao, Y., Zhang, G., Setunge, S., Shi, L., 2021. A critical review of combined natural ventilation techniques in sustainable buildings. Renew. Sustain. Energy Rev. 141, 110795.

Zhang, T., P.A, Chen, D., Cai, J., 2020. Discussion on the influence factors of high-rise building heat load calculation, 07 Shanxi Architec. 46, 101–103 (In Chinese).

Zhang, X., Weerasuriya, A.U., Tse, K.T., 2020. CFD simulation of natural ventilation of a generic building in various incident wind directions: comparison of turbulence modelling, evaluation methods, and ventilation mechanisms. Energy Build. 229, 110516.

Zhang, X., Zhang, R.R., 2001. Actual ground-exposure determination and its influences in structural analysis and design. J. Wind Eng. Ind. Aerod. 89 (11), 973–985.

Zhao, M., T.G, Chen, Z., Zhu, H., 2002. Comparison of different slope grading systems and ground slope spectrum in the loess hilly and gully area, 04 Soil and Water Conser. Bullet. 33–36 (In Chinese).